TAMPEREEN TEKNILLINEN YLIOPISTO
TAMPERE UNIVERSITY OF TECHNOLOGY

NAZANIN KARIMI

DIRECT LASER WRITING OF FLUORESCENT MICROSTRUCTURES CONTAINING SILVER NANOCLUSTERS IN POLYVINYL ALCOHOL FILMS

Master of Science Thesis

Examiner: Dr. Juha Toivonen
Examiner and topic approved by the Council of the Faculty of Natural Science
on June 4, 2014

ABSTRACT

KARIMI, NAZANIN: Direct Laser Writing of Fluorescent Microstructures containing Silver Nanoclusters in Polyvinyl Alcohol Films
Tampere University of Technology
Master of Science Thesis, 57 pages
April 2015
Master's Degree Program in Science and Bioengineering
Major: Nanotechnology
Examiners: Dr. Juha Toivonen, M.Sc. Puskal Kunwar

Keywords: Metal nanoclusters, Polymer, Photopolymerization, Direct laser writing, Spectroscopy, Photoluminescence, Photostability.

Metal nanoclusters (NCs), consisting of a few to few hundred atoms with dimensions comparable to Fermi wavelength of electrons, exhibit significant molecular behavior. As a result of quantum confinement effect, electrons which freely move in bulk metals become confined to the spaces that can be as small as a few atom spacings. This confinement of electrons gives rise to unique properties such as discrete energy levels, strong photoluminescence, and considerable chemical reactivity. Therefore, synthesis of stable NCs could open the door to engineer novel nanomaterials with tunable characteristics with a potential for numerous scientific and industrial applications. However, NCs are not realized in practice as they are less stable than nanoparticles (NPs). Hence, using proper stabilizer matrices is a requirement for synthesis of NCs. NCs can be formed and stabilized in solutions by reducing dissolved metal ions in the presence of organic molecules such as proteins, and polymers. Moreover, direct laser writing (DLW) is shown to be a promising technique in fabrication and stabilization of metal NCs in polymer and glass matrices.

In this thesis, we demonstrate the fabrication of highly fluorescent microstructures containing silver NCs in polyvinyl alcohol (PVA) thin films using DLW technique. Polymer thin films were prepared by spin-coating aqueous solutions of PVA containing silver nitrate on glass substrates. Single-photon DLW were performed on silver-polymer films by tightly focusing the continuous-wave (CW) laser beam of wavelength 405 nm, and scanning the sample against the constant laser beam. Photoluminescence of the structures, dependence of the fluorescence intensity on silver concentration and writing laser power, and photostability of the fabricated microstructures were studied by using different optical characterization methods. Atomic force microcopy (AFM) was used to estimate the thickness of the film, investigate the surface topology, and measure the line width of the written structures.

The results showed broadband photostable fluorescence emissions from NCs at visible wavelengths. Dependence of the fluorescence intensity on silver concentration confirmed that the presence of silver in the polymer film is the cause of the bright luminescence. AFM analysis of the written structures depicted the formation of grooves with depths of 35 ± 3 nm in a thin film of 58 nm thickness. Moreover, it was observed that the breadth of the grooves, as well as the emitted fluorescence intensity, increased with the writing power. The silver NCs fabricated in this method were similar in character to NCs stabilized in organic solutions. Moreover, the results were consistent with those obtained from the silver NCs fabricated in poly-methacrylic acid (PMAA) films by using two-photon DLW technique. The outcomes of this work indicated that single-photon DLW can be a useful method to sythesize highly fluorescent metal NCs with any desired pattern in various kinds of polymer resins.

PREFACE

The Master of Science thesis ‘Direct Laser Writing of Fluorescent Microstructures containing Silver Nanoclusters in Polyvinyl Alcohol Films’ was done in Optics Laboratory of Department of Physics at Tampere University of Technology.

I would like to express my sincere gratitude to Dr. Juha Toivonen for providing me the great opportunity of working on this interesting topic in Applied Optics group, and for his guidance and supervision during the project. Special thanks to M.Sc. Puskal Kunwar for patiently helping me to organize the experiments and sharing his helpful knowledge and experience. I am also grateful to M.Sc. Jukka Hassinen from Aalto University Nanomicroscopy Center for his help in AFM measurements, and the Optoelectronic Research Center for letting me use their clean room facilities.

I would like to gratefully acknowledge Prof. Martti Kauranen, who gave me the chance of working in the friendly environment of Optics Laboratory.

Finally, this thesis is dedicated to my parents whose limitless love and support have always been the key to my success, and my dear Behnam for all his encouragement, positive attitude, and affection.

Nazanin
Tampere, Finland
April 2015

CONTENTS

LIST OF ABBREVIATIONS AND SYMBOLS

AFM	Atomic Force Microcopy
BSA	Bovine Serum Albumin
CV	Cyclic Voltammetry
CW	Continuous-wave
DFT	Density Functional Theory
DLW	Direct Laser Writing
DNA	Deoxyribonucleic Acid
DP	Degree of Polymerization
EA	Electron Affinity
EDS	Energy Dispersive x-ray Spectroscopy
EMCCD	Electron Multiplying Charge Coupled Device
GC	Glassy Carbon
HOMO	Highest Occupied Molecular Orbital
IR	Infrared
LED	Light Emitting Diode
LUMO	Lowest Unoccupied Molecular Orbital
MEMS	Microelectromechanical Systems
MMD	Molar Mass Distribution
NC	Nanocluster
NIR	Near-infrared
NP	Nanoparticle
PAMAM	Poly-amidoamine
PEI	Polyethylenimine
PES	Photoelectron Spectroscopy
PI	Photo-initiator
PMMA	Poly-methacrylic Acid
PPI	Poly-propyleneimine
PVA	Polyvinyl Alcohol
PVAc	Polyvinyl Acetate
PVP	Poly-vinylpyrrolidone
PS	Photosensitizer
QD	Quantum Dot
SEM	Scanning Electron Microscopy
SPR	Surface Plasmon Resonance
TPA	Two-photon Absorption
UV	Ultraviolet
vdW	van der Waals
vis	visible
1PP	Single-photon Photopolymerization
2D	Two-dimensional
2PP	Two-photon Polymerization
3D	Three-dimensional

A	Affinity of phase transition
a	Activity of particles in a solutiom
α	Absorption coefficient
c	Concentratiom
D	Density of states
d	Distance
ΔG	Total free energy change
ΔG_S	Surface free energy change
ΔG_V	Volume free energy change
δ	Absorption cross-section
E	Energy
E_F	Fermi energy
E_{kin}	Kinetic energy of electrons
ε_d	Dielectric constant
Φ_0	Polymer initiation
γ	Surface energy per unit area
h	Planck constant
ħ	Reduced Planck constant
I	Light intensity
J	Rate of nucleation
k	Wave number
k_B	Boltzmann constant
χ	Electric susceptibility
λ	Wavelength of light
M	Monomer unit
M_n	Macromolecule contains n monomers
M_P	Molecular weight of polymer
M_0	Molecular weight of repeating units in a polymer
m	Electron mass
μ	Chemical potential
N_A	Avogadro number
ν, ω	Light frequency
P	Polarization
PI^*	Excited photo-initiator
PS^*	Excited photo-sensitizer
R	Gass constant
R·	Radical
r	Radius of a spherical cluster of atoms
r^*	Radius above which the affinity of the transformation is positive
ρ	Volume fraction occupied by nanoparticles
S	Supersatiration parameter
S_0	Ground electronic state
S_1	Excited singlet state
T	Temperature
$T_{d,0}$	Initial polymer decomposition temperature
$T_{d,1/2}$	The temperature of half decomposition of polymer
T_1	Triplet state
t_{ind}	Induction time
V	Molecular volume
V_e	Classical electrostatic potential

V_{eff}	Effective potential
V_i	External potential caused by ions
V_m	Molar volume
V_{xc}	Exchange potential
W	The energy change per unit time, per unit volume
wt	Weigth

1. INTRODUCTION

It has been a long time since the significance of nanotechnology was remarked by Feynman in 1959 when he presented his famous lecture entitled “there is plenty of room at the bottom”. Developing new techniques for synthesis of nanomaterials, as well as advanced tools for their manipulation and characterization, has fueled the development of nanoscience and technology during last years. [1] The major demand of this field has been shrinking the dimensions of materials in order to make an advantage from the unique properties they exhibit in nanometer scale. According to their characteristic length scales, nanomaterials are classified to nanoparticles (NPs) with diameters larger than 2 nm, and nanoclusters (NCs) with the size smaller than 2 nm (comparable with the Fermi wavelength of electrons). [2] The ability to synthesize and characterize such ultra-small clusters, has opened the door to a new field which builds a bridge between atomic and NP behavior. Also, it leads to the contribution of different disciplines of physics, chemistry, materials science, biology, medicine, and environmental sciences. [3]

The main focus of this thesis work is on metal NCs, which have been studied by researchers from a long time ago. Due to quantum confinement effect, metal NCs exhibit novel optical, electrical, and catalytic properties significantly different from not only their bulk counterparts, but also larger NPs. One of the remarkable features of such molecule-like metal NCs is their significant photoluminescence, which has made them attractive materials for lots of studies. More specifically, synthesis and characterization of water-soluble noble metal NCs (e.g., gold and silver) have attracted lots of attention since 1990s. Their intense fluorescence, low toxicity, and ultra-fine size have proposed them as interesting materials for applications in optical data storage, sensing, bioimaging, and biolabeling. [2, 4] Great interest in taking advantage of metal NCs properties have motivated researchers to work intensively on developing the methods of NCs synthesis. The main difficulty of synthesizing metal NCs is their strong tendency to aggregate and form larger particles, which no longer exhibit the significant properties such as strong luminescence [5]. Therefore, great effort has been made to find feasible and affordable techniques for growing NCs and stabilizing them in order to prevent their agglomeration. Successful synthesis of fluorescent metal NCs in various organic and inorganic stabilizing matrices such as polymers [5], dendrimers [6], deoxyribonucleic acid (DNA) [7], glasses [8], and zeolites [9] have been reported. In this thesis work, steric stabilization approach by utilizing polymer agents is used to synthesize silver NCs. Polymers have been shown to be excellent matrices to grow strongly fluorescent metal NCs. Aqueous solutions of a variety of polymers such as

polyphosphate, polyacrylate, poly-methacrylic acid (PMMA), and polyvinyl alcohol (PVA), which are known for stabilization of colloidal particles, can be appropriate for this purpose [5, 10, 11]. The mostly used process for polymer stabilization of NCs includes reduction of metal ions to zero-valent atoms within the polymer solution, followed by coalescence of polymer molecules surrounding the NCs through polymerization process. This thesis is concerned with photo-induced polymerization process, which has become a well-known and beneficial method of polymerization, as a consequence of developments in laser technology. Single-photon absorption by using conventional high-frequency laser sources, and multi-photon absorption by utilizing near-infrared (NIR) femtosecond (fs) lasers are two primary mechanisms of photopolymerization. By employing the technique of direct laser writing (DLW), either of these two mechanisms can be applied to selectively polymerize the polymer films and fabricate patterned structures containing fluorescent metal NCs.

DLW has been a very beneficial tool to modify, add, and subtract materials from nanometer to millimeter scales for a variety of applications in photolithography, microelectronics, nanophotonics, biomedicine, etc. In general, DLW refers to a technique used to create two-dimensional (2D) or three-dimensional (3D) structures without any need of masks or pre-existing templates. Moreover, development of laser technology has reinforced DLW as a fast and cost-effective way to produce novel structures and devices. [12] Fabrication of silver NC in inorganic matrices through DLW was reported several years ago by Bellec et al. [8] and De Cremer et al. [9]. Recently, Kunwar et al. have published the first employment of DLW in an organic matrix [5]. They fabricated 2D fluorescent structures containing silver NCs in PMMA thin films through the two-photon absorption process. In general, fabrication of 3D structures is more feasible by using two-photon absorption approach while 2D structures can be constructed by applying either of two processes. Therefore, the concern of this thesis is fabricating such photostable fluorescent microstructures in organic matrices by using single-photon absorption mechanism. The organic matrix we use for this purpose is PVA, a water-soluble polymer with excellent film-forming and stabilizing properties. Thin films of PVA containing metal particles can be readily prepared on glass substrates through simple methods such as spin-coating. Afterward, DLW on polymer films can be done by collimating and tightly focusing the light beam into the resin. Typically, patterning is attained by either scanning the laser beam over a fixed surface or moving the sample within the fixed beam [12].

This thesis consists of eight chapters including the introduction. Chapter 2 provides information about NCs, specifically metal NCs, principles of cluster formation and growth, important electronic, optical and chemical properties of NCs, and the methods of cluster stabilization. General aspects of polymers with a focus on PVA properties, introducing spin-coating as a method of polymer processing, and conditions leading to degradation of polymers are included in Chapter 3. After presenting some fundamental information about polymers, the process of polymerization with a particular attention to photo-induced polymerization and its primary mechanisms (single-photon and

two-photon polymerizations) are discussed in Chapter4. The theoretical background of the thesis is followed by Chapter5, which provides information about experimental methods and setups used for the sample preparation, DLW of silver NCs, and their characterization. The results of the experiments are presented in Chapter6, and some of them are further discussed in Chapter 7. Finally, Chapter 8 concludes this thesis work, and it is followed by the list of references used for this project.

2. NANOCLUSTERS

In physics and chemistry the term “Nanocluster (NC)” refers to a group of few to few hundreds atoms of the same element, usually a metal, bonded closely together [3]. The dimension of NCs is typically less than 2 nm comparable with Fermi wavelength of electrons. In this dimension, metal NCs exhibit typical molecular behavior leading to privileged electronic, optical and chemical properties. [11]

The properties of metals significantly change when they scale down from bulk to small NCs. Freely moving electrons in the conduction band of bulk metals are responsible for their electrical conductivity and optical reflectance. As the dimensions of metal shrink down to the size of NPs, the metallic features disappears. Instead, a surface plasmon resonance (SPR) effect, which is the characterization of metal NPs, causes intense colors when particles interact with light. When the size of metal is further reduced to less than 2 nm, the plasmonic properties also disappear. The continuous density of states in bulk metals breaks down into discrete energy levels. As a result of electronic transitions between discrete levels, NCs exhibit features such as significant light absorption and emission. In fact, metal NCs act as a bridge between metal atoms and NPs. [11, 13]

Significant properties of metal NCs such as ultra-small size and strong fluorescence make them attractive materials for applications in single-molecule studies, fluorescence imaging, fluorescence sensing, optical data storage, and labeling. Particularly, silver NCs which are synthesized in organic matrices have a great potential to be used as fluorescent biolabels due to their biocompatibility, intense brightness, and photostability. Moreover, as the optical response of the NCs depends on their interaction with organic scaffolds, they can be utilized as sensitive probes. [13]

NCs can be synthesized in solutions by reducing metal ions from dissolved metal salt using chemical reductants, light, or γ-rays. However, the growth of the NCs needs to be stabilized since they have a large tendency to aggregate and decrease their surface energy. Therefore, utilizing a stabilizer agent to prevent NCs agglomeration is essential in order to use their significant properties for real applications.

In this chapter, the physical principles of formation and growth of NCs are briefly explained. Afterward, the electronic structure of metal NCs is studied that is followed by introducing their important optical and chemical properties. Finally, different approaches for stabilization of metal NCs are introduced.

2.1 Formation and growth of nanoclusters

Understanding the details of NCs growth process is beneficial to control their desired properties. NCs can be synthesized using various methods such as chemical reduction, photoreduction, thermal decomposition, ligand reduction and displacement from organometallics, metal vapor synthesis, and electrochemical synthesis [14]. Chemical reduction and photoreduction of metal ions in suitable encapsulating media such as dendrimers, polymers, DNA, etc. are the most common methods of NC synthesis [13]. Preparation of wet chemical NCs and NPs using chemical reduction have been used for several decades [15]. For the first time, this reduction method was applied by Faraday in 1857 during his studies on gold sols [16]. That includes the reduction of metal ions to a zero-valent state in an aqueous or organic media and stabilizing them to avoid further growth of particles [5, 15]. In addition to chemical reduction, photoreduction methods have been proved to be very useful to synthesize noble metal NCs. Activation with light enables control of the reduction process without introducing undesired impurities, and the interaction can be initiated homogenously. [17]

After reduction of metal ions, the nucleation of atoms occurs that is followed by the growth of clusters by adding colloidal particles to the formed seed nucleus [15]. In order to understand the growth of NCs, one needs to comprehend the classical nucleation process which is the perquisite for studying NCs and NPs growth [18]. Classical theory of nucleation describes the condensation of vapor molecules to primary spherical liquid droplets. This theory has been expanded to crystallization from solutions as well. [19] Nucleation can be either spontaneous (homogeneous nucleation) or induced (heterogeneous nucleation). Homogeneous nucleation happens in the absence of any impurity species while heterogeneous nucleation occurs when nucleation is affected by the presence of impurities. [20] In primary homogeneous nucleation, solute atoms or molecules in a supersaturated solution combine to generate clusters as the growth of a nucleus reduces the Gibbs free energy of the system [19, 21]. Nucleation initiates as a result of thermodynamic imbalance between the liquid phase and solid phase leading to the phase transition. Affinity of the transition A is a thermodynamic force that causes the phase shift. It is the result of the difference between chemical potentials μ of the two phases:

$$A = \mu_1 - \mu_2 \,. \tag{1}$$

Chemical potential is defined by

$$\mu = \mu_0 + RT \ln a \,. \tag{2}$$

Here, μ_0 is the standard potential, R is the gas constant, T is the temperature and a is the activity of particles in the solution. Chemical potential of a spherical cluster with radius r is

$$\mu(r) = \mu_2 + (2\gamma/r)V_m\,, \tag{3}$$

where μ_2 is the chemical potential of the bulk material, γ is the interfacial tension or surface energy per unit area, and V_m is the molar volume. Thus, the affinity of the phase transformation is

$$A = \mu_1 - (\mu_2 + (2\gamma/r)V_m)\,. \tag{4}$$

The value of the thermodynamic force A has to be positive in order to convert liquid phase to the solid phase. That means that the phase change happens only when particles are adequately large. For a certain $\Delta\mu = |\mu_1 - \mu_2|$, the critical radius r^* is defined as a radius above which the affinity of the transformation is positive and the NC will grow [18, 20]

$$r^* = (2\gamma/\Delta\mu)V_m\,. \tag{5}$$

$\Delta\mu$ defines the difference between values of free energy per mole for bulk states of two phases. If the cluster grows into a sphere with radius r, the total free energy change ΔG is sum of the change in surface free energy ΔG_S and change in free energy of the cluster volume ΔG_V

$$\Delta G = \Delta G_S + \Delta G_V = 4\pi r^2\gamma - (4\pi r^3/3V_m)\,\Delta\mu\,. \tag{6}$$

Then, the free energy change for the cluster with critical radius is defined by

$$\Delta G^* = (16\pi/3)(\gamma^3 {V_m}^2/\Delta\mu^2)\,. \tag{7}$$

The rate of nucleation, which is the number of particles nucleated per cubic centimeter per second, is described by Arrhenius equation:

$$\begin{aligned} J &= A\,\exp(-\Delta G^*/k_B T) \\ &= A\,\exp\left[-(16\pi/3)\left(\gamma^3 {V_m}^2/\Delta\mu^2 k_B T\right)\right], \end{aligned} \tag{8}$$

where k_B is the Boltzmann constant. Considering the equation (2), by using a valid approximation, the chemical potential difference can be defined as a function of supersaturation parameter S

$$\Delta\mu = RT\ln S\,, \tag{9}$$

where $S = c/c_0$ is a ratio of the solute concentration c to the saturation concentration c_0. Then the nucleation rate as a function of supersaturation degree is

$$J = A.\exp\left[-(16\pi/3)\left(\gamma^3 V^2/{k_B}^3 T^3\{\ln S\}^2\right)\right], \quad (10)$$

$V = V_m/N_a$ is the molecular volume where N_a is the Avogadro number. [20] Applying the equation (9) in equations (5) and (7), one can conclude for $S > 1$, increasing S results in decreasing the critical size and consequently the energy barrier. Thus, the probability of growing sufficiently large clusters which can overcome the barrier and become stable will be enhanced. That means a higher rate of nucleation, which is evident from equation (10). [18] This equation is the standard expression for primary homogeneous nucleation rate which shows three major variables: the temperature, the supersaturation degree, and the interfacial tension [18, 20]. The most cited example of applying the nucleation theory to cluster formation is the work of LaMer in 1950s on the formation of sulfur sols [22]. Turkevitch was the first one who proposed the stepwise formation and growth of gold NCs based on nucleation soon after LaMer in 1951 [23]. Later, thermodynamic and kinetic studies with the help of modern analytical techniques have considerably modified the model, and several reviews have been published including those complementary theories. Nowadays, development of computational chemistry has made it possible to design sophisticated NCs exhibiting desired behaviors for specific applications. [15]

Different experimental methods were also used to measure the kinetics of cluster formation during last decades. In 1960s Nielson performed some experimental measurements and proposed an empirical description of the primary nucleation process using an induction time t_{ind}

$$t_{ind} = k \times c^{1-\rho}, \quad (11)$$

where k is a constant, c is the concentration of the supersaturated solution, and ρ is the number of particles required to create the critical nucleus [24]. Since then, several spectroscopic techniques have been developed to measure kinetics of NCs formation and their dimensions. Dynamic light scattering to acquire information about clusters size in solutions, ultraviolet (UV)-visible spectroscopy, and x-ray spectroscopy to study the kinetics of cluster formation are examples of those methods. However, there is no precise quantitative experimental description of metal NCs formation kinetics in solutions. Most of the experimental methods are able to measure kinetics of larger clusters not the nucleation process. [25]

Nucleation and growth of the clusters have been profoundly studied theoretically. Although the classical nucleation theory is a logical starting point to investigate the formation of metal NCs, it is a simplified explanation of a complicated process. This theory treats the nucleus as a bulk material and assumes that the surface free energy of the cluster is the same as that for an infinite planar surface. Both of these assumptions need to be modified when studying small clusters including few atoms. [25] Moreover, the energy of cluster formation determined based on this theory, does not include any information about the structure of the cluster. Early stage mass spectroscopy

experiments have resulted in prominently high concentration of clusters with specific numbers of atoms called magic numbers. [19] These particles composed of sequentially packing layers of atoms around a single atom and possess hexagonal or cubic close packing structures which built stepwise by nucleation of specific numbers of atoms (magic numbers). The allowed number of particles which can be added to a full-shell cluster including n shell to construct the (n+1) shell is determined by $10n^2+2$. This formula suggests 13, 55, 147, 309 atoms and so on for the size of clusters. [14, 15] Most of the nanoclusters possess geometries close to that of magic clusters. Since the maximum number of metal-metal bonds is formed in full-shell geometries, they are more stable. [14] However, classical theory is not able to predict this phenomenon [19].

Furthermore, the systems in classical theory are considered to be in equilibrium and nucleation occurs slowly. Fast nucleation systems with extreme collapse cannot be studied only using the classical theory. Moreover, the nucleation rate in the theory is defined by addition of one single atom to the sub-critical nucleus. In the case of multi atoms addition like cluster-cluster collisions, reconsidering the formulation is essential. Thus, to overcome these weaknesses and provide a comprehensive formulation, complementary methods determine the binding energies of clusters with various geometries through ab initio quantum mechanical calculations. The concentration development of different sized clusters with time can be also predicted based on a population balance theory of nucleation considering all possible collisions of clusters and associated energies. Thus, the required time to grow the highest concentration of a cluster with a particular size is predictable. It allows tuning experimental conditions in order to maximize the concentration of a cluster possessing a desired size. [19] This ability of size tuning is significant since the electronic structure, optical absorption, and catalytic properties of NCs are strongly influenced by their dimensions. Some of these size dependent features will be discussed in the following.

2.2 Electronic structure of metal nanoclusters

Continuous shrinking the size of bulk metals to NCs causes significant changes in their properties since the bulk behaviors are due to an infinite number of their building blocks [26]. Electronic structure of nanoscale particles with dimensions more than 1 nm depends on the number of atoms they include, and is intermediate between the electronic structure of molecules and that of the bulk materials. Ultra-small NCs with a size less than 1nm, exhibit a typical molecular behavior while there are still some structural relations to their bulk counterparts [27, 26]. Therefore, in contrast to bulk metals that behave based on classical laws, NCs containing few atoms follow quantum mechanical rules; and, their properties strongly depend on the exact number of their atoms. [27]

In bulk materials, orbitals with similar energy states combine and make electronic energy bands. In the case of semiconductor and insulating crystals, there is always an energy gap between the valence and conduction bands, and bonding varies from weak

van der Waals (vdW) to strong covalent or ionic bonds. In bulk metals, the band gap disappears at Fermi level, and metallic bonding arises from delocalization of electrons. The valence band is completely occupied by valence electrons and the conduction band as a result of overlap with the valence band is partially filled with electrons, which are responsible for conductivity of metals. By ceaselessly decreasing the size of metal particles to nanoscale dimensions, the overlap of valence and conduction bands weakens and a band gap similar to that in semiconductors appears. [3] Therefore, small NPs always exhibit an energy gap between the highest occupied molecular orbital (HOMO) and lowest unoccupied molecular orbital (LUMO) either they consist of metallic or nonmetallic elements. Consequently, nanoscale metals do not contribute in metallic bondings as their corresponding crystals do. Further miniaturize the size of the metal particles, results in formation of the NCs with more or less discrete energy levels. [3, 27] At this point, the size of a metal NC is comparable to the De Broglie wavelength of electrons with energy comparable to Fermi energy (E_F) of metals. Thus, the NC behaves analogous to a quantum dot (QD) for electrons. [28] As a result of quantum size effect, the free carrier is now quantum confined and behaves according to quantum mechanical 'particle in a box' model. The solutions of the Schrödinger equation for such a system are bounded standing waves in a potential well, which associate with quantized and discrete energy levels. [29] The structure of energy levels in this dimension will change by altering the size of the NC [28]. Further shrinking the size of the NC to less than 1 nm yields to a typical molecular situation [27]. Figure 1 illustrates the electronic structure development from overlapping energy bands in bulk metal to discrete levels in a molecule-like situation.

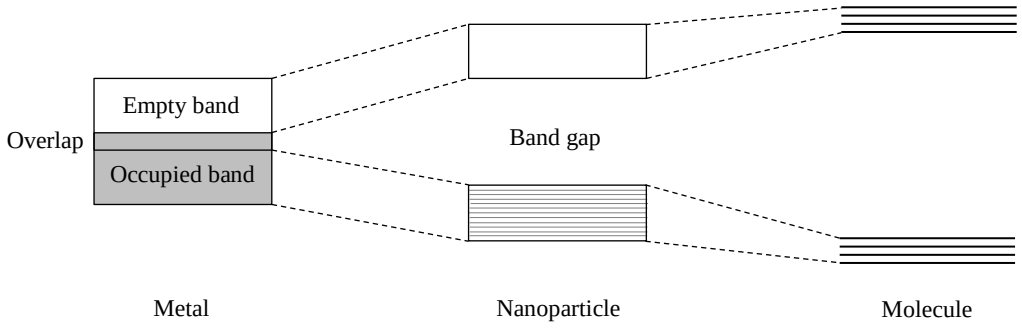

Figure 1: The development of electronic energy levels from bulk metal to molecule.

In order to understand the development of electronic structures from continuous to discrete levels, the electronic changes of a solid as its dimensions shrink from the bulk state to a quantum dot shall be studied. A 3D piece of metal can be considered as a crystal that is extended infinitely in x, y, z directions $(d_{x,y,z} \to \infty)$, and contains free electrons. Each direction corresponds to a standing wave in $\vec{k}$-space with the wave numbers k_x, k_y, and k_z. Each of the states k_x, k_y, and k_z can be occupied by maximum two electrons according to Pauli's exclusion principle. As a consequence of periodic boundary conditions in an infinite solid, the allowed wavenumbers meet the

condition $k_{x,y,z} = \pm n_{x,y,z}\Delta k = \pm n_{x,y,z}\,{}^{2\pi}/_{d_{x,y,z}}$, where n is an integer number. Since $d_{x,y,z}$ in a bulk solid is large, Δk tends toward zero. The energy of free electrons is proportional to the square value of the wavenumber, $E(k_{x,y,z}) = \left({}^{\hbar^2}/_{2m}\right) {k_{x,y,z}}^2$, where $\hbar$ is the reduced Planck constant, and m is the electron mass. That leads to quasi-continuous energy states and the density of states $D_{3d}(E)$, which varies with square-root of the energy ($D_{3d}(E) \propto E^{1/2}$). If the size of metal in any of three infinite directions decreases to a few nanometers, the electrons cannot move freely anymore, and they will be confined in that particular direction resulting to quantized energy states. Reducing the size of one dimension to few nanometers leads to a system called two-dimensional electron gas or quantum well. For instance, in a 2D solid extended infinitely along x and y directions, k_z is allowed to contain only discrete values. The smaller d_z, the larger Δk_z between quantized states. The energy states diagram is still quasi-continuous while the density of states corresponds to a step function. Therefore, the original electrons of the metal which were able to move freely in three dimensions now are allowed to move in only two dimensions. Diminishing the size of the solid along the second direction, for example, y dimension yields the confinement of electrons in two directions. The system is called one-dimensional electron system or quantum wire. The values of Δk in y and z directions are quantized, but it is not the case along x direction. Therefore, the energy diagram is a parabola with $\Delta k_x \to 0$. The density of states depends on $E^{-1/2}$ and for each discrete k_y and k_z state result in a hyperbolic curve that exhibits continuous distribution of k_x states. The next step is to shrink the size of x direction as well in order to include a zero-dimensional quantum dot system. Now, the electrons are confined in all three dimensions and only discrete values for $k_{x,y,z}$ are acceptable. Therefore, the energy levels are completely quantized, and the density of states contains delta peaks. In a QD system, the last few metallic electrons are enclosed in three dimensions and because of quantum size effects they behave such as particles in a box. These electrons are responsible for significant change of physical and chemical characteristics of metal clusters. [26, 27, 29] Figure 2 indicates the evolution of density of states as a function of the electrons energy from a bulk metal to a nanocluster.

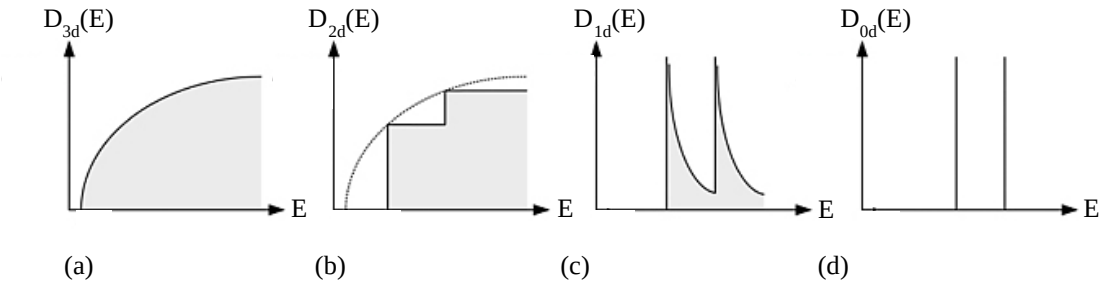

Figure 2: The density of states as a function of electron energy in (a) a three-dimentional bulk metal, (b) two-dimentional, (c) one-dimensional, and (d) zero-dimensional systems. [30]

Different qualitative and quantitative theoretical approaches have been utilized to study NCs, and their success has depended on the property under investigation. It is cooperation between theoretical and experimental efforts that has led to significant advances in the field during last few decades. Metals and particularly transition metals provide a unique occasion to study the passage from bulk to molecular state and eventually to mononuclear complexes. All the substantial and unique properties of these NCs are due to the dramatic reduction of freely mobile electrons during the size decrement from bulk to cluster. Both simple metal and transition metal NCs can be explained with similar theoretical models. Many of the typical properties of metal NCs have been observed for transition metals as well as for simple metals. However, simple metals are easier to investigate theoretically and have been the subject of lots of theoretical studies regarding the electronic structure of small NCs. The theoretical outcomes about the effects of size reduction in main group metal NCs are applicable for transition metal NCs as well. [26]

To determine the electronic structure of simple metal NCs, the jellium model has been vastly used as a convenient theoretical method. The properties of simple metal NCs are governed by delocalized sp orbitals; thus, the formation of electronic structure and shell closing effect is very similar to that of free atoms. However, NCs of typical transition metals are not influenced by shell effects as their d orbitals are partially filled. The compact d shell electrons with strongly spin-dependent correlation dominate the electronic structure of such NCs [31]. Therefore, studying the electronic properties of transition metal NCs is more complicated than that for simple metals, and simplified jellium model is not enough to describe their electronic structure. [3, 32] However, experiments on noble metal NCs indicated that the electronic shell effect is present similar to the case of alkali metal NCs [32]. The reason is that d shells of noble metals are completely filled by ten electrons, and the valence shell contains one electron in s orbital. [31] It has been realized that some magic numbers define the electronic shell effects in these metal NCs similar to the case of simple metals. In first approximation models, the valence electrons in alkali metal clusters behave as free electrons moving in an effective potential well with spherical symmetry around the NC center which is defined by

$$V_{eff}(R) = V_i(R) + V_e(R) + V_{xc}(R)\,, \tag{12}$$

where $V_i(R)$ is the external potential caused by ionic background and can be easily determined by jellium model. The second contributor $V_e(R)$ is the classical electrostatic potential of the electron cloud, and $V_{xc}(R)$ denotes a non-classical potential due to exchange and correlation effects between electrons. The approximately spherical effective potential causes highly degenerate electronic shells. Electrons occupy the shells 1S, 1P, 1D, 2S, … . The maximum number of electrons that can exist in each shell is 2(2l+1) where l is the orbital angular momentum. The most stable clusters are those with the precise number of electrons required to fill the shells. The experimentally observed magic sizes for stable NCs also correlate with $N = 2, 8, 18, 20, 40, 58, ...$ electrons that can be described by shell filling progression. The electron cloud in NCs with open shells is not spherical which brings a more complicated geometry of such NCs. Thus, the model needs some modifications to consider these spheroidal deformations as well. The substantial stability of closed shells still has a significant role in the revised models; however, its magnitude is reduced. The spheroidal deformations in small NCs lead to an almost complete lifting of the orbital degeneracy. [32]

In addition to theoretical models, lots of experiments have been conducted to understand the evolution of NCs electronic structures. One method to study the development of energy structure is to monitor the alteration of HOMO-LUMO gap with respect to the NC size. Photoelectron spectroscopy (PES) and velocity map imaging are two experimental procedures to measure the evolution of the energy gap [3, 32]. In PES method, the kinetic energy of a photo-detached electron from a negative ion NC is measured. The difference between incident light energy and electron kinetic energy $\hbar\omega - E_{kin}$ (where ω is the fixed light frequency) gives a direct estimation of the binding energy of the orbital. Therefore, the PES spectra illustrate the electron energy levels of the NC and HOMO-LUMO gap. Every NC has its own corresponding spectrum. The photoelectron threshold can give an estimate of electron affinity (EA) of the X_N^- NC that is the difference between energies of neutral and anionic clusters:

$$EA = E(X_N) - E(X_N^-)\,. \tag{13}$$

If X_N is a closed shell NC, the detached electron is coming from the lowest unoccupied molecular orbital (LUMO) of X_N. Thus, photoelectron threshold expresses shell effects. Information regarding the electronic structure of the noble metal cluster anions (Cu_N^-, Ag_N^-, and Au_N^-) can be obtained directly from PES measurements. Measured PES threshold detachment energies of Ag_N^- and Cu_N^- indicate drops between $N = 7$ and $N = 8$, also between $N = 19$ and $N = 20$. It again reminds the shell closing numbers $(1S)^2(1P)^6$ and $(1S)^2(1P)^6(1D)^{10}(2S)^2$ respectively. [32] Velocity map imaging is another common technique to study the electronic structure of NCs by determining the asymmetry of photo-ejected electrons and eventually, the corresponding orbitals [3].

Similar results to alkali metal NCs have encouraged researchers to apply the spheroidal jellium model for noble NC with various sizes. This model can explain some properties of noble metal NCs by neglecting d electrons. However, the form of valence electrons in noble metals is so different from that of alkali metals because of localized d electrons and s-d mixing. [32] Therefore, the applicability of the closed shell model for the case of noble metals has been studied by several experimental and theoretical physicists. Smalley and coworkers utilized ultraviolet electron spectroscopy to investigate the effects of 3d electrons of copper cluster anions Cu_N^- with N up to 410 [33]. The results indicated a large peak which was around 2 eV larger than threshold peak and evolved moderately with the particle size. The position of the peak for the small NCs resembled the position of d level of copper atom. Therefore, the peak was ascribed to the ejection of 3d electrons. Smooth change of 3d features with the size is due to the fact that 3d electrons are core-like and weakly affected by the details of the NC surface. As N increases the onset of the 3d band sharpens implying the formation of the crystalline. By using density functional theory (DFT) or quantum chemical methods the detailed structure of coinage metal NCs has been theoretically characterized with prominent agreement with the experiments. In 1990s, Fujima and Yamaguchi performed DFT calculations on Cu_n clusters with N up to 19 for different model structures [34]. Massobrio et al. operated such calculations to study smaller NCs with $N \leq 10$ [35]. Moreover, using quantum chemistry, Baushclicher and coworkers have conducted all electron, and relativistic core potential calculations to estimate electron affinities of copper, silver, and gold NCs [36]. The structure of NCs with medium and large sizes with N up to several tens to hundreds has been studied by X-ray powder diffraction methods and calculated utilizing semiempirical many-atom potentials by Garzon et al. [37].

The above mentioned studies are just few examples of vast efforts to perceive the behavior of NCs. Advances in experimental methods, as well as computational techniques, have provided for more precise investigations of the electronic structure of nanoscale clusters. Better understanding of NCs electronic features has enabled to control and tune the desired properties of NCs for a variety of applications. Consequently, other unique properties such as optical and catalytic characteristics can be explained more accurately. The next sections of this chapter are devoted to effects of electronic structure on such properties.

2.3 Optical properties

The optical properties of materials are affected by their electronic structure and band gap. Shrinking the size of the metal to dimensions smaller than 50 nm will eventuate in a remarkable change of its properties as a result of quantum confinement of electrons which move freely in the bulk state. [27] One of the major optical properties of metal NPs is their intense surface plasmon resonance (SPR) in the visible region [38]. The optical properties alter even more dramatically when the size of metal particles

decreases to less than 2 nm [27]. One of the main differences in optical properties of small NCs and NPs is the absence of localized SPR peak in absorption spectra of metal NCs. [5, 17] The absorption coefficient α for particles smaller than $\lambda/20$ is described by Mie scattering theory in the electric dipole approximation [39]:

$$\alpha = \frac{18\pi\epsilon_d^{3/2}}{\lambda} \cdot \frac{\rho . \epsilon_2}{[\epsilon_1 + 2\epsilon_d]^2 + \epsilon_2^2}, \quad (14)$$

where λ is the wavelength of the incident light, ρ denotes for the volume fraction occupied by NPs, ϵ_d is the dielectric constant of the host material, and $\epsilon_1(\omega)$ and $\epsilon_2(\omega)$ are real and imaginary parts of the dielectric function of the metal, respectively, $\epsilon(\omega) = \epsilon_1(\omega) + i\epsilon_2(\omega)$. When $\epsilon_1 + 2\epsilon_d = 0$, the absorption peak will be observed at the SPR frequency. The SPR depends implicitly on the particle size. Increasing the size leads to the growth and sharpening of the resonance peak. Usually, NCs with diameters less than 2 nm do not contribute to the SPR absorption peak since the volume fraction of the clusters decreases significantly. Therefore, Mie's theory is no longer applicable for NCs. [39] Instead, lower density of electronic states in ultra-small metal NCs leads to molecule-like optical properties such as strong broadband fluorescence emission with high degree of photostability [5, 17].

Noble metals are appropriate examples to investigate the difference between optical properties of NPs and NCs. Gold and silver NPs exhibit characteristic surface plasmon absorption bands with size-dependent position and intensity. The SPR is a result of confining the conduction electrons in both ground and excited states to dimensions below the electron mean free path ($\sim$20 nm). Further confinement of electrons, a second critical size that is the Fermi wavelength of electrons ($\sim$0.7 nm) can be reached. This results in molecule-like discrete transitions. [40] Usually, large Ag NPs demonstrate the absorption feature at around 420 nm while Ag NCs with diameters less than 2 nm exhibit different absorption profile. This absorption feature provides a useful tool to estimate the size of the particles using ultraviolet-visible (UV-vis) absorption measurements. As an example, Figure 3 illustrates UV-vis absorption spectra of Ag NPs and Ag NCs measured by Lu and Chen [41]. As indicated in the Figure 3, there is a broad absorption peak related to the NPs at 427 nm, which is the characteristic of Ag NPs. However, the absorption peak of NCs is rather sharp and red-shifted to 503 nm. The position of the latter peak is in a good agreement with UV-vis absorption feature of Ag_7 NC with size around 0.7 nm. [41]

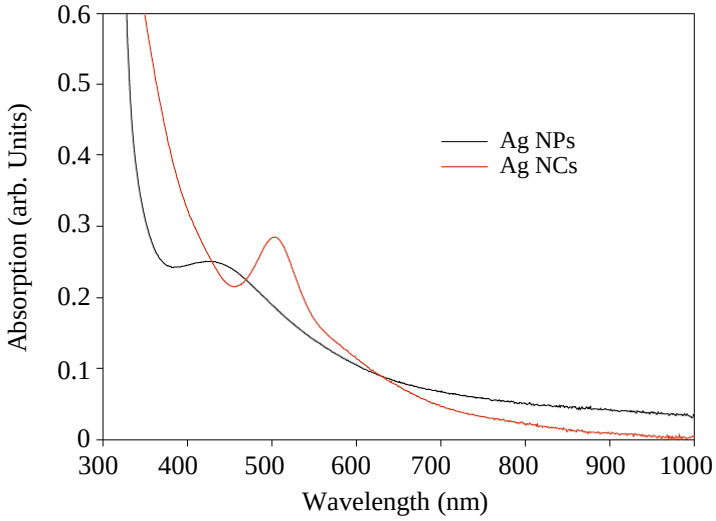

Figure 3: UV-vis absorption spectra of silver NPs (black curve) and silver NCs (red curve). [41]

The noble metal NCs photoluminescence property is associated with the excitation-recombination process related to d-band electrons. The absorbed photon excites an electron from the narrow d-band to an empty sp orbital above the Fermi level. The next step is the carrier relaxation in both bands, and finally, the radiative recombination of an electron close to the Fermi level to the highest unoccupied orbital results in visible to NIR emissions. The simple energy diagram of this excitation-recombination process is illustrated in Figure 4. For the first time, luminescence of water-soluble metal NCs attracted attentions in 1990s. Improvements in synthesis technologies have resulted in successful fabrication of silver and gold NCs with high fluorescence quantum yield. [4] By utilizing spherical jellium model for gold NCs, researchers have obtained that the dependence of the emission energy on the number of atoms in a NC (N) can be fit by a simple scaling relation $E_F/N^{1/3}$, where E_F is the energy of Fermi level. Increasing the number of atoms in a NC, results in decreasing of the emission energy. [40]

Strong fluorescence emission of noble metal NCs, mainly gold and silver NCs, has made them promising materials for a variety of applications such as labeling, imaging, and sensing. To produce such photo-stable small NCs, stabilizing them by different ligands is a requirement. The role of ligand molecules in the enhancement of NCs fluorescence emission is very significant as they have influence on the structure and electronic properties of NCs. It has been reported that the HOMO-LUMO gap of the NC can be tailored when it is coated with various ligands [3]. In fact, tuning the emission wavelength is possible by changing the coating molecules. It is achievable through template-based synthesis methods using various templates such as dendrimers, oligonucleotides, proteins, polyelectrolytes, and polymers. The protected fluorescent NCs have been observed to be more stable against photobleaching in comparison with organic dyes. [4, 42]

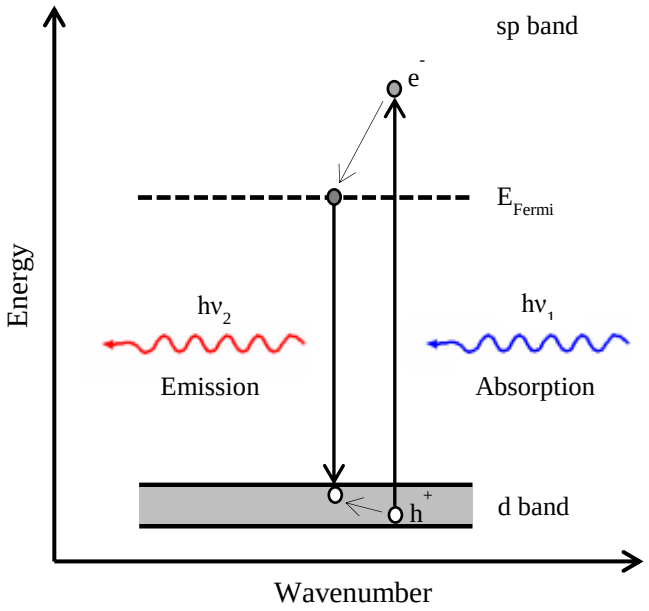

Figure 4: Energy diagram depicting the mechanism of photoluminescence in noble metal NCs.

In addition to significant fluorescence emission, metal NCs exhibit large enhancement effect on the Raman scattering signals of surrounding molecules in charge-transfer mechanisms [43]. Raman scattering is a light-matter interaction, which provides valuable information about the structure and composition of materials. This phenomenon occurs when an incident light scatters elastically from vibrational quantum states of molecules. During this process, energy is exchanged between photons and vibrational excitations. The change in the photon energy may cause a shift in the frequency of the scattered light. Vibrational information of the molecules can be obtained from the frequency shift between the excitation and scattered light. However, Raman signal is usually weak, particularly from the surfaces containing small amount of molecules. It has been shown that electronic coupling between molecules producing Raman scattering effect and metal NCs can modify the scattering process. Electronic levels of the molecules may become shifted or broadened, or new levels appear due to charge transfer between molecules and metal NCs leading to an enhancement in Raman scattering signal. The presence of the metals in the system may also change the polarizabilility of the surrounding molecules and increase the Raman scattering efficiency. [44]

2.4 Chemical reactivity

In addition to significant optical properties, metal NCs have been observed to exhibit exclusive reactivity as a result of their large surface-to-volume ratio [3]. A high percentage of NC atoms exist on the surface, and their arrangement do not necessarily resembles that of the bulk metals. Low mean coordination number of surface atoms causes the valence band to become narrower. Thus, the density of states close to the Fermi level decreases and the band center is transferred toward higher energies. [3, 14,

45] It results in a strong electron affinity and different chemical reactivity from that of the bulk metals. The electron affinity of metal NCs can be as large as 10 eV while the highest electron affinity among elements of the periodic table belongs to chlorine which is 3.61 eV. NCs with such a large electron affinity are called super-halogens and consist of a metal atom at core enclosed by halogen atoms. A good example of super-halogens is platinum hexafluoride (PtF_6). It is possible to enhance the electron affinity even further by having a metal atom at core surrounded by super-halogens; these species are called hyper-halogens. [3]

Interaction of transition metal NCs with molecules such as nitrogen (N_2) can be utilized to investigate the geometry of the NCs. It has been reported that a metal NC exposed to the gas molecules under a varying pressure can adsorb variable number of gas molecules. Based on the measurements results, the binding of the cluster and gas molecule and eventually the structure of the cluster can be determined. [3] Furthermore, utilizing powerful mass spectrometric techniques enables the accurate examination of metal NCs reaction with different molecules [46].

Coinage metals are usually considered as catalytically inert materials for lots of applications. Their low activity in chemical reactions is due to their completely occupied d-bands leading to higher activation barriers than those for metals with partially filled d-bands. Nevertheless, NCs of these metals have exhibited high catalytic activity in many experiments. For instance, high catalytic activity of gold NCs in reactions such as low temperature CO oxidation and NO reduction has been reported. In energy structure of low-coordinated coinage metal atoms, there is a narrow gap between d-band and the Fermi energy level. As a result, the NC surface consists of much more active sites to adsorb oxygen molecules compared to the closed packed counterparts. The fraction of surface atoms in the particles strongly depends on their size. Metal NCs exhibit much more catalytic activity than NPs. Several experiments have been conducted on Au and Ag NCs and NPs to investigate the influence of metal particles size on their catalytic activity. [41]

Lu and Chen have performed electrochemical cyclic voltammetry (CV) measurements on nanoscale silver particles with various sizes. Their results have indicated that small NCs with diameters around 0.7 nm exhibit higher catalytic activity to oxygen reduction reaction than NPs (3.3 nm). Figure 5 illustrates the CV results for Ag NPs/ glassy carbon (GC) electrode (b), and Ag NCs/GC electrode (a) in 0.1 M KOH solution which is saturated with oxygen or nitrogen molecules. The potential scan rate for all measurements is 0.1 Vs^{-1}. On both electrodes when the solution is saturated with oxygen molecules, the reduction current is more remarkable than that for the nitrogen saturated solution. That indicates the high catalytic activity of silver NPs and NCs to oxygen reduction. Moreover, the voltammetric measurements indicated that the electrocatalytic activity of small Ag NCs to ORR is superior to that of the large NPs. They obtained -0.28 V and -0.13 V onset potentials for Ag NPs/GC and AG NCs/GC electrodes, respectively. It means that onset potential of ORR for 0.7 nm NCs is 150 mV more positive than that for 3.3 nm NPs. Furthermore, it can be seen from Figure 5.a that

the oxygen reduction current density at -0.80 V is around -0.25 mA cm^{-2} for NPs electrode. However, as shown in Figure 5.b, it increases to -1.50 mA cm^{-2} at NCs electrode which is five times higher than the former. Further measurements also resulted in higher mass activity of small NCs compared to NPs. [41]

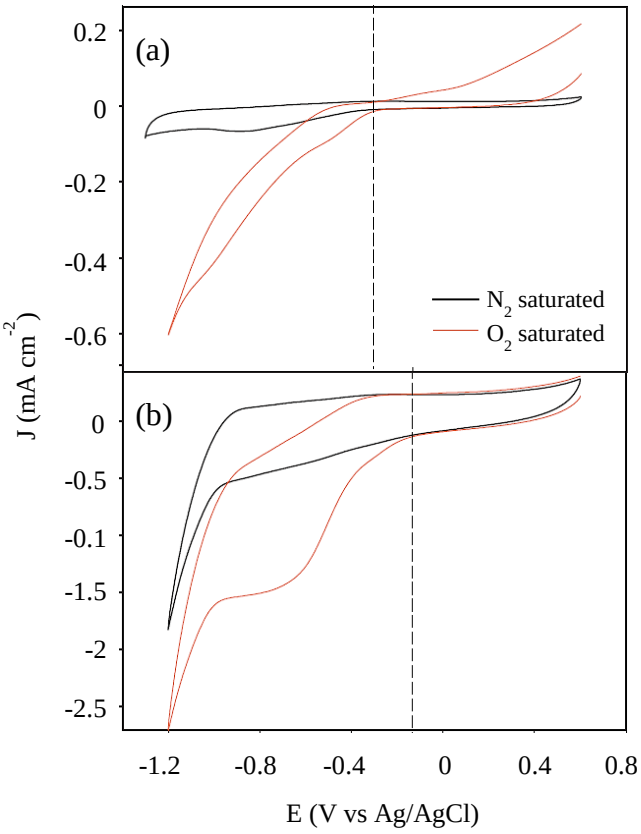

Figure 5: Cyclic voltammograms of Ag-NPs/GC (a) and Ag-NCs/GC (b) electrodes in 0.1 M KOH solutions saturated with nitrogen and oxygen molecules. Current is normalized by electrochemically active surface areas, and Ag/AgCl was used as the reference. [41]

2.5 Stabilization of metal nanoclusters

As mentioned in chapter2.1, in order to synthesize metal NCs, a salt or a complex of the corresponding metal is dissolved in a solvent and reduced to a zero valent state. However, synthesizing nanoclusters in aqueous solutions is usually difficult because clusters strongly tend to agglomerate and interact with each other to decrease their surface energy. It results in the formation of NPs which no longer exhibit molecule-like properties especially fluorescence emission. [5, 47, 48] Moreover, nucleation of metal particles is a complicated phenomenon which is a result of cooperation of several factors such as the difference between the redox potentials of metal salt and the reducing agent, reaction temperature, rate of addition, and stirring rate. In order to obtain a monodisperse NC, the nucleation process has to be completed before the growth stage begins. Therefore, short nucleation time is a requisite. If the nucleation and growth steps overlap, growth time varies for different nucleation sites, and the result is

an undesired particle size distribution. In order to avoid these phenomena and produce hydrosol and organosol stable NCs, one needs to stop the growth process at the right moment to prevent the generation of larger crystals. The growth is stoppable by using ligand molecules coordinating to the surface atoms. [15] Ligand molecules control the particle growth thermodynamically rather than kinetically, and may be present in the solution during the reduction process or added after that [15, 48]. In our case study which is silver NCs, the former one has been used. Moreover, chemical interaction between the stabilizer molecules and surface atoms of the metal NCs leads to considerable effects on the NC electronics structure. Therefore, the nature of the stabilizer agent controls the fluorescence emission of the protected metal NCs. [47]

The fundamental cause of NCs aggregation is an attractive vdW force between particles. Therefore, the stabilization occurs when this attractive force is dominated by a stronger repulsive one or weakened via covering the NCs. [15] There are different methods of stabilization depending on the type of the covering layer: electrostatic (inorganic), steric (organic), and electrosteric stabilizations. Electrostatic stabilization includes the adsorption of ions to the electrophilic metal surfaces. A created electrical double layer leads to the Coulombic repulsion force between existed particles. The electrostatic potential must be high enough to protect particles from aggregation. Steric stabilization occurs when the metal particle is surrounded by layers of large organic molecules such as polymers. Polymer stabilizers create abundant weak bonds with the surface of the NC rather than few strong bonds. Some stabilizers exhibit both electrostatic and steric effects. That leads to a very reliable process to stabilize NCs. Electrosteric stabilization includes adsorbing of bulky molecules such as polymers and surfactants at the NC surface. These molecules shield the particles and at the same time make strong electrostatic bond to the metal surface. [14, 15] Figure 6 illustrates the schematic images of electrostatic and steric stabilization methods.

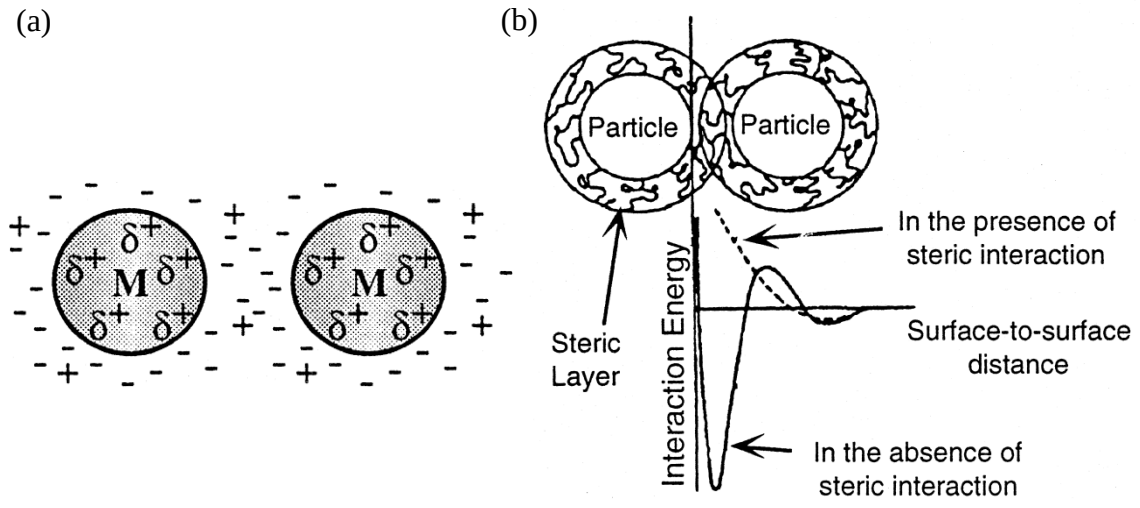

Figure 6: Schematic images of two stabilized particles using (a) electrostatic stabilization, and (b) steric stabilization by adsorption of polymer molecules [14].

Using the different modes of stabilization, researchers have studied the synthesis of NCs in a variety of stabilizer agents. One of the mostly used stabilizers is DNA oligonucleotides, mainly to stabilize silver NCs [47]. For the first time, Dickson and coworkers reported the synthesis of water-soluble Ag NCs in DNA templates [49, 50]. Since then, lots of studies have been performed on DNA-templated Ag NCs because of their bright and photostable fluorescence emissions. By utilizing different DNA sequences, it is possible to tune the fluorescence emission of silver NCs. Proteins and peptides are another type of protective molecules which enable intercellular generation of fluorescent noble metal NCs. Furthermore, using dendrimers as stabilizers have been beneficial because of their uniform composition and structure. The most commonly used dendrimers are poly-amidoamine (PAMAM) and poly-propyleneimine (PPI). Recently, using polymer stabilizers have also attracted a lot of attentions. As an example, Poly-methacrylic acid (PMAA), which is a well-known polymer with numerous carboxylic acid groups has been proved to be a promising stabilizer for the formation of stable Ag NCs. Strong affinity of silver ions or silver surfaces to carboxylic acid groups makes this polymer a unique environment to grow NCs. Other polymers such as polyethylenimine (PEI), and poly-vinylpyrrolidone (PVP) are also used as protective ligands. [47] In this thesis, Polyvinyl alcohol (PVA) was used for the formation and stabilization of water soluble Ag NCs.

The emission spectrum of noble metal NCs is highly affected by the protective molecules. Therefore, by choosing appropriate stabilizers, the desired emission of gold and silver NCs for different applications can be obtained. [4] For instance, it has been reported that quantum confined water-soluble gold NCs stabilized by PAMAM emit blue light with a high quantum yield [51]. Green and red-emitting NCs have been also synthesized by tuning the ligand molecules. Le Guével et al. have synthesized silver and gold NCs with red emission in bovine serum albumin (BSA) using wet chemistry [42]. They investigated the influence of pH on growth and emission of the clusters. Moreover, Ag NCs stabilized by single-strand DNA has been reported to emit various colors in visible-NIR region [52]. Photogeneration of fluorescent silver NCs in polymer microgels has been first reported by Kumacheva et al. [53], and was followed by other researchers to overcome the limitations regarding generation of larger non-fluorescent nanoparticles. For instance, Shang and Dong used PMAA solution as a template for the photogeneration of Ag NCs, and they observed obvious color changes from colorless to dark red in the NCs emissions [17]. Therefore, the emission wavelength of metal NCs not only is affected by their size, but also depends significantly on the nature of the encapsulating environment. [4]

3. POLYMERS

Polymers are macromolecules that exist in a variety of natural and synthetic forms such as enzymes, DNA, concretes, plastics, adhesives, coatings, clothes, papers, and are main ingredients of soil [54]. They are useful materials for most of the recent technologies mainly because of their large molecular size. When a molecule is large, it includes lots of intermolecular van der Waals (vdW) contacts to its neighbor molecules. Sum of the vdW forces keeps molecules tightly together and provides mechanical strength to the polymeric material. [55] Technologies such as computer chips, portable batteries, superconductors, optical fibers, liquid crystals, medicines, drug delivery system, synthetic blood, skin, and limbs use different kinds of polymeric materials [54].

The word ‘polymer’ refers to a chain molecule consisting of structural repeating units called monomers, which are connected together by covalent bonds through polymerization process [56]. If the fundamental repeating units comprise a single identifiable precursor, the polymer is a homopolymer. If a polymer molecule consists of two or three different types of basic structures, then we have a copolymer. The composition of copolymers may vary from well-ordered repetition to a random distribution. The number of repeating units mainly in homopolymer molecules is called the degree of polymerization (DP). The molecular weight of a polymer M_P is then the molecular weight of the repeating units M_0 multiplied by DP, $M_P=(DP)M_0$. A polymer with low molecular weight and low mechanical strength is called oligomer and consists of at least two monomer units. [55]

Two major factors determining the properties of a polymeric material are the chemical identity of its monomers and its microstructure. Microstructure is the arrangement of atoms along the chain that is fixed during the polymerization and cannot be altered without breaking the covalent bonds. [57] It is formed by a skeleton, which may have a linear chain, branched chain, or network architecture with lots of atomic groups attached to the backbone. When each repeating unit of a polymer molecule is attached to other two repeating units, the molecule is linear. Polystyrene is an example of linear polymers. If some of the repeating units in the polymer molecule are also attached to other monomer residues, that are different from the repeating monomers, the molecule is called branched polymer. For instance, vinyl acetate has such a structure. By chemically linking linear or branched polymers together, the so-called network polymers can be obtained. This process is called cross-linking. Finite-sized polymers also contain some end groups which are different from the repeating structures. Usually, the exact structure of end groups is not known, and their influence on physical properties is negligible. [55, 56] The spatial arrangement of a polymer molecule that is

determined by the relative location of its monomers is called the polymer conformation. After the polymerization, a single flexible molecule may embrace various conformations depending on the flexibility of the chain, and interaction of monomers with surroundings. [57]

One important classification of polymers related to their structure divides them to addition molecules and condensation molecules. The repeating unit in condensation polymers lacks some certain atom(s), which are present in primary monomers building the polymer molecule. Polyesters or polyamides are examples of condensation polymers. Addition polymers consist of repeating units with the exact structure of the monomers. Polyethylene and polyvinyl alcohol are examples of addition polymers. Condensation polymers are formed through a step-wise polymerization process while addition polymers are generated by a chain process. [58] A brief explanation of polymerization processes is presented in 4.1.

If all polymer molecules in a substance contain the same number of monomers, the polymeric material is monodisperse that is the case for most of the natural polymers such as proteins. However, synthetic polymers are mainly polydisperse. The polydispersity of a particular polymer is described by its molar mass distribution (MMD). [57] The MMD provides information regarding the average molecular size, and the regularity of the distribution. The chemical structure and the pattern of MMD control almost all of the other properties of a polymeric material. Some of these properties such as cohesive forces, packing density, and molecular mobility are directly affected whereas the others like morphology and relaxation phenomena are indirectly influenced by chemical structure and MMD. [56]

As mentioned in Chapter 2.4, several polymer molecules provide an appropriate environment to grow and stabilize nanoclusters. Because of their large molecular weights, the chain dimensions of polymers are comparable to the range of van der Waals attractions, and this is useful for steric stabilization methods [59]. In this thesis, we used polyvinyl alcohol (PVA) as a stabilizer for silver nanoclusters (NCs). Therefore, in the following subchapters, molecular structure and general properties of PVA are described, which is followed by polymer processing methods. Finally, the effects of ambient conditions on polymeric materials are presented.

3.1 Polyvinyl alcohol

Polyvinyl alcohol (PVA) is a synthetic water-soluble resin with excellent film forming, emulsifying, stabilizing and adhesive properties [60]. The main chain of vinyl polymers in general contains carbon atoms with single bonds and other additive substituents such as chlorine, fluorine, or hydroxyl groups [61]. PVA in particular is a linear molecule, and its relatively simple chemical structure consists of vinyl alcohol (C_2H_4O) monomer and a pendant hydroxyl group [62]. The repeating structure of PVA is shown below:

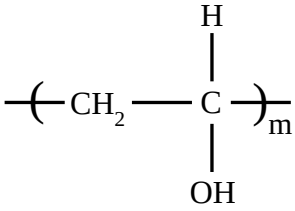

where m refers to the number of the repeating units [55]. Presence of hydroxyl groups makes it a hydrophilic polymer [61, 63]. PVA has high biodegradation rate, and the hydrogen bondings between molecules lead to a high mechanical strength [60, 64]. It can be well dissolved in water but not in common organic solvents [63]. The viscosity of aqueous PVA solutions varies with PVA concentration and temperature of the solution [65].

PVA is synthesized since 1924 when Herman and Haehnel reported the formation of PVA through saponification of polyvinyl acetate (PVAc). Vinyl alcohol is not a stable molecule and usually exist in the form of its tautomer, acetaldehyde. Thus, to produce PVA, first vinyl acetate monomers are polymerized to PVAc; then, it is converted to PVA through hydrolysis. Sometimes, the hydrolysis does not result in a complete conversion of PVAc to PVA. Consequently, the produced material is a copolymer of PVA and PVAc. Various types of PVA grades from partially hydrolyzed to fully hydrolyzed grades with broad range of MMD are commercially available. The physical characteristics including water solubility, mechanical strength, gas permeability, adhesion, diffusion, thermal and stabilizing properties depend significantly on the crystallinity level of the polymer. Degree of crystallinity is determined by the hydrolysis level and the average molecular weight of the molecule. Partially hydrolyzed grades containing residuals of acetate groups exhibit small degrees of crystallinity. It results in a low strength of the material and high solubility in water compared to fully hydrolyzed grades. Highly hydrolyzed PVA with degrees of hydrolysis above 98.5% are dissolved in water if the temperature is well above 70˚C. [62, 66] Table 1 provides a summary of the influence of molecular weight and degree of hydrolysis on physical properties of PVA.

Features such as aqueous solubility, stabilizing ability, biocompatibility, biodegradability, non-toxicity, and environmental friendliness make PVA an attractive material for a variety of applications. It is vastly used in textile industries, paper products manufacturing, food packaging, adhesives, and coatings. Particularly, it is a safe polymer for biomedical and pharmaceutical purposes. Moreover, due to its excellent film-forming properties, PVA is used as high oxygen barrier films, membranes, and polarizing films. [60, 63, 67]

Table 1: Influence of the molecular weight and degree of hydrolysis on physical properties of PVA.

Increased solubility Increased flexibility Increased water sensibility Increased ease of solvation	Increased viscosity Increased tensile strength Increased water resistance Increased solvent resistance Increased adhesive strength
MOLECULAR WEIGHT decreasing — increasing  HYDROLYSIS %	
Increased solubility Increased flexibility Increased water sensibility Increased adhesive to hydro-phobic surfaces	Increased water resistance Increased tensile strength Increased solvent resistance Increased adhesive to hydro-philic surfaces

3.2 Polymer processing

Polymer processing is defined as utilizing specific methods to convert raw polymeric materials, usually present in the form of powders or granules, to desired products with particular microstructures, shapes, and properties. In order to fabricate microstructures from polymers, specific methods like spin-coating and polymer spraying are used for making thin films of polymer solutions on substrates such as glass. The next step is polymerizing the desired parts of the polymer film through polymerization processes like laser writing, UV curing, etc. [68] In this thesis, we used spin-coating to prepare thin and uniform films of silver containing PVA solution on glass substrates.

Spin-coating of solutions in order to form homogeneous thin films on a substrate is an ordinary non-equilibrium process mostly used to produce photoresists. The primary processes involved in spin-coating are fluid dispense, spin-up, fluid outflow, and evaporation. [69] First, solution is deposited on a clean substrate. There are two methods of dispensing fluid on the substrate, static dispense, and dynamic dispense. Static dispense includes depositing of a small amount of the solution near the center of the fixed substrate. Depending on the size of the substrate and viscosity of the fluid, the deposited amount can range from 1 to 10 cc. If the fluid is dispensed on a low-speed rotating substrate, the process is called dynamic dispense. The latter is useful when the

fluid has poor wetting abilities. After deposition of the solution, the next step is spin-up which includes accelerating the substrate and fluid to a final desired speed. Typically chosen spin speeds are in the range of 1500-6000 rpm depending on the characteristics of the fluid and substrate. The spinning speed can last from 10 seconds to several minutes. It is the cooperation of the spinning speed and spinning time which determine the final thickness of the layer. Usually, higher speeds and longer time result in thinner films. The principle of thinning the film during the rotation is that the centrifugal force spreads the fluid outward and ejects the excess of the liquid out of the edge of the substrate. Meanwhile, the evaporation of the solvent results in drying the resin, and consequently increasing the viscosity of the fluid. Viscosity increases up to the point that the centrifugal force can no longer disperse the resin, and a final equilibrium thickness is achieved. [70, 71]

Controlling the spin speed is one of the important factors on the layer thickness. It has influence on both the degree of centrifugal force applied to the resin, and the velocity and turbulence of the air above the resin. Acceleration of the substrate during first seconds of spinning also has a significant effect on the film uniformity. It provides a twisting force to the resin and disperses the fluid around the area. In addition to the system variables, the nature of the resin is also responsible for the film characteristics. Properties of the solution such as volatility, viscosity, surface tension, drying rate, and solid concentration highly affect the drying of the resin and consequently the final thickness. Ambient conditions such as humidity and temperature of the air around the solution are other determinant factors. During the process, air flow and turbulence above the layer has to be minimized or kept constant. It can be achieved by using closed bowl design spin coaters. This system minimizes the influence of ambient humidity change and variations of air flow around the substrate. After spinning, if the solvent is a nonvolatile liquid such as water as in our case, the resin needs to be kept in a desiccator for final drying. The drying step is essential to stabilize the film before using it. [71] Finally, a uniform polymer film with a desired thickness is achievable by taking care of all of the determinant parameters.

After preparing polymer films through spin-coating, the polymer needs to be cured and hardened through polymerization process. One of the well-known techniques for microfabrication in polymer films is photo-induced polymerization by using UV curing or direct laser writing (DLW). The main mechanism of photopolymerization is photo-induced reaction of monomers or oligomers to produce polymeric materials (this polymerization method is explained in detail in Chapter4.) [72]. After fabrication of the desired structures in polymer films through polymerization step, the unexposed regions can be washed out by using photoresist developers. [73]

3.3 Effects of ambient conditions on polymeric materials

Particular ambient factors such as heat, light, or chemicals can lead to the decomposition of a polymer and alter its properties including molecular weight, tensile

strength, shape, color, and other important characteristics. Therefore, to have stable polymeric materials for a long time, one needs to be familiar with the causes of degradation and their effects on the polymer properties. [74, 75]

Thermal resistance is one of the most important properties of polymers since it controls the mechanical properties, persistence, spectral stability, and life cycles of polymers [76]. Even highly resistant polymers may undergo degradation at high temperatures. At this condition, the primary chemical bonds are broken and polymer degrades down to its monomers. In principle, thermal degradation can be determined by dissociation energy of chemical bonds. There are three types of thermal decomposition mechanisms: chain depolymerization, random decomposition, and degradation through substituent reactions. Chain depolymerization is the reverse process of chain polymerization that includes the release of monomer units from one end point of a chain or at a weak link. Weak links may exist as a result of chain defects or impurities. Random degradation means the fragmentation at random points along the chain and is considered as the reverse of polycondensation. The detached segments are usually large compared to monomer units. Chain and random decompositions may occur separately or in combination. In the case of vinyl polymers, usually, chain depolymerization is the dominant degradation process. Degradation by substituent reactions happens through modification or elimination of substituents, which are connected to the polymer backbone. For most of the polymers, thermal pyrolysis begins at temperatures around 150-200˚ C and increases with increasing the temperature. Two major experimental indices that characterize the thermal degradation are the temperature of initial decomposition, and the temperature of half decomposition. The initial decomposition temperature ($T_{d,0}$) is the temperature at which the weight loss of the polymeric material due to heating becomes measurable. The temperature of half decomposition ($T_{d,1/2}$) is defined as the temperature at which the weight loss reaches the 50% of its ultimate value. These characteristic temperatures depend on the rate of the heating. According to the reports, $T_{d,0}$ and $T_{d,1/2}$ of PVA at a standardized rate of heating (normally around 3 K/min) are 493 K and 547 K respectively. The characteristic temperatures change to higher values by increasing the rate of the heating. [74]

Ambient light can be another typical cause of polymer degradation. The required activation energy to break an individual covalent bond is in the range of 165-420 kJ/mol. That amount of energy corresponds to the wavelengths from 280 nm to 720 nm. Thus, near ultraviolet radiation (300-400 nm) has the adequate amount of energy to break most of the covalent bonds except very strong ones such as C-H and O-H. Ideal polymers with perfect structures do not absorb wavelengths longer than 300 nm. However, most of the polymers contain impurities and structural defects which absorb light, and that results in photochemical degradation when exposed to the sunlight. The exact nature of the impurities is usually unknown, but it has been accepted that they are either carbonyl groups or peroxides. UV-induced degradation can be prevented by utilizing UV-absorbers which transform the absorbed energy into heat, or by quenchers (for example nickel chelates), which dissipate the electronic excited states

of impurities. [74] In addition to UV-radiation, some other sources such as ion beams, gamma rays, or electron radiation may also be used to degrade polymers for some purposes [75].

Chemical decomposition may also occur as a result of reactions with surrounding components. The most important reagent of chemical degradation is oxygen. Photo-oxidation, caused by radiation, and thermal oxidation, caused by thermal energy are two primary processes. At room temperatures, the oxidation appears after a long time because of slow reaction rate. However, factors such as electromagnetic radiation or thermal energy accelerate the oxidation by formation of radicals. In the case of photo-oxidation, radical formation occurs through absorption of light photons and in thermal oxidation through temperature change, shear effects or residues of catalysts. The rate of thermal oxidation can be estimated by measuring the amount of oxygen absorption at a particular temperature. Both oxidation processes can be avoided by using antioxidants. Addition of UV absorbers is also a useful way to prevent photo-oxidation. In addition to oxidation, other kinds of chemical degradation like hydrolytic degradation may occur. Hydrolytic degradation takes place when hydrolysis reactions in water or acids are responsible for breaking the bonds. If the ambient temperature is high enough, the rate of decomposition is fast. Mechanical properties including tensile strength, elongation, and impact strength may be destroyed severely as a result of all chemical degradation processes. In some polymers, it may also lead to discoloration. [74]

In biological environments, certain micro-organisms and enzymes can motivate the degradation of polymers. The biodegradability depends on the molecular weight, molecular structure, and crystallinity of the polymer. The higher the molecular weight, the lower the biodegradability. Investigations on degradation of PVA in various environments and conditions have resulted in high degrees of biodegradation, which can be a desired property for many applications. Among vinyl polymers produced industrially, PVA is the only one that can undergo degradation by micro-organisms. [75] The biodegradation of PVA can occur as a result of a random chain division process in which a two-enzyme catalyzed oxidation is responsible for bond breaking. [77]

4. PHOTOPOLYMERIZATION

Photopolymerization includes a light-induced chain chemical reaction to transfer small unsaturated molecules in the liquid phase to macromolecules in solid phase within a polymerizable resin. Different light sources from UV, visible to IR region can be employed to initiate the polymerization. Fundamental components required for polymerization are monomers or oligomers in the liquid material. However, direct formation of reactive species in monomers through light absorption is not an efficient process. Therefore, presence of photo-initiators (PIs) is required to generate reactive species, which initiates the polymerization reaction when excited by light. Photosensitizers (PS) can also be added to extend the spectral sensitivity. They absorb the incident energy of a wavelength that PI cannot absorb and then transfer the required excitation energy to the PI. This reaction is called sensitized photo-induced polymerization. Photo-induced polymerization is commonly considered as an environmentally friendly technology because of low energy requirements, low-temperature procedures, and no release of volatile organic compounds. [78, 79]

Photoinitiated polymerization by UV lamps is a well-known method not only for conventional applications such as adhesives, coating, and inks but also for recent technologies in photonics, optoelectronics, and microelectromechanical systems (MEMS). Moreover, due to the developments in laser technology and possibility of high localization of laser energy, laser-induced polymerization has become an attractive subject for many scientific areas. This technique has been studied widely for potential applications in biomedicine, bones and tissue engineering, nanotechnology, direct laser patterning of microcircuits, holographic devices, information recording media, and so on. [79, 80, 81] In the following, the principles of photopolymerization process are explained, that is followed by presenting single-photon and two-photon induced DLW.

4.1 Polymerization processes

Polymerization is a chemical process during which monomers are covalently bonded together [57]. Two primary mechanisms of polymerization are step-growth and chain-growth processes [58]. In step-growth mechanism, functional groups of monomers react with each other in a stepwise process to form dimers, trimers, and other low molecular weight oligomers to eventually build polymers with high molecular weights. Sometimes, these stepwise reactions are accompanied by elimination of some small molecules, which result in the formation of condensation polymers such as polyesters. [54, 82] Usually, small molecules such as water are released during condensation polymerization. To reach high molecular weight in this process, an

extremely efficient reaction with no side reactions is required. Moreover, molecules must have at least two reactive functional groups in order to grow through a stepwise polymerization. Another major mechanism is chain-growth polymerization, which includes the sequential addition of monomers to the growing chain. Vinyl molecules such as PVA are usually synthesized via this process. Based on the initiation procedure and nature of the propagating chain, the chain-growth is classified to anionic, cationic and free radical processes. [83] The most important process in polymer synthesis is chain-type radical polymerization. Almost 50% of all synthetic polymers are made through radical processes. This method is popular because of several reasons including convenient temperature range (20-100℃) and minimal need for purification of monomers and solvents. Radical polymerization can be carried out in bulk, solution, emulsion, aqueous suspensions, and other environments. Another important benefit is that a large range of monomers can be polymerized using this mechanism. [84] Ionic type photopolymerizations are not used as commonly as radical type ones. Low curing speed, low viscosity, small shrinkage after polymerization, and drastic post-irradiation dark polymerization are some drawbacks of ionic processes. [72]

The primary process in a photo-induced polymerization involves chain-type free radical reactions. The main steps of chain polymerization are Initiation, Propagation, and Termination. [72] These processes are explained in detail below.

Quantum yield of photopolymerization is defined by the number ratio of polymerized monomers to photons required for the polymerization. Ideally, it can reach several thousand as a result of chain reactions represented by

$$M \xrightarrow{M} M_2 \xrightarrow{M} M_3 \cdots M_{n-1} \xrightarrow{M} M_n \,, \tag{15}$$

where M is the monomer unit, and M_n is the macromolecule contains n monomers. However, in practical systems the quantum yield of monomers and oligomers is small. By adding PIs, the efficiency of polymerization can be enhanced. PIs are low-weight light sensitive molecules in the photoresist, which are reduced to initiating radicals through photon absorption. This process is called ‘photoinitiation’, which is the first and most important stage of photopolymerization. Initiation process that is used to generate a radical is defined by

$$PI \xrightarrow{h\nu} PI^{*} \rightarrow R\cdot, \tag{16}$$

where PI^{*}, and $R\cdot$ denote for an intermediate state after absorbing a photon ($h\nu$), and the produced radical, respectively. In many cases, the PI cannot absorb the energy of the incident light. Instead, light is absorbed by PS molecules and then the energy is transferred to the PI. In this case, the photoinitiation step is described by the following reaction: [72]

$$PS \xrightarrow{h\nu} PS^* \cdots \xrightarrow{PI} PI^* \rightarrow R\cdot \tag{17}$$

Afterwards, the active initiating species react with monomers and oligomers generating monomer radicals which combine with other monomers in a chain reaction. Thus, a more realistic polymerization process in the presence of PIs is described by

$$R\cdot + M \rightarrow RM\cdot \xrightarrow{M} RMM\cdot \cdots \rightarrow RM_n\cdot \tag{18}$$

This step is called ‘chain propagation’. The propagation continues until two radicals face each other. The last step ‘termination’ includes stopping the expansion through either of two following reactions: [72]

$$RM_n\cdot + RM_m\cdot \rightarrow RM_{m+n}R \tag{19}$$
$$RM_n\cdot + RM_m\cdot \rightarrow RM_n + RM_m \tag{20}$$

Two major techniques of photopolymerization are single-photon and two-photon polymerizations. As it is evident from the names, the only difference between these two processes is the method of providing energy to activate the initiators. [72] The fundamental principles of these two mechanisms and a brief comparison of them are presented in the following.

4.2 Single-photon photopolymerization

When polymerization process is initiated through absorption of single photon in UV or near-UV region, the process is called single-photon photopolymerization (1PP). [72] The principle of single-photon absorption can be described by a linear dipole transition. [85] A single photon of energy $h\nu_1$ (where ν_1 is the light frequency) excites the PI molecule from the ground state (S_0) to an excited single state (S_1). Usually, relaxation takes place through intersystem crossing to a triplet state (T_1). Photochemical reactions such as radical formation occur from T_1 as shown in a simple Jablonski diagram in Figure 7. [86]

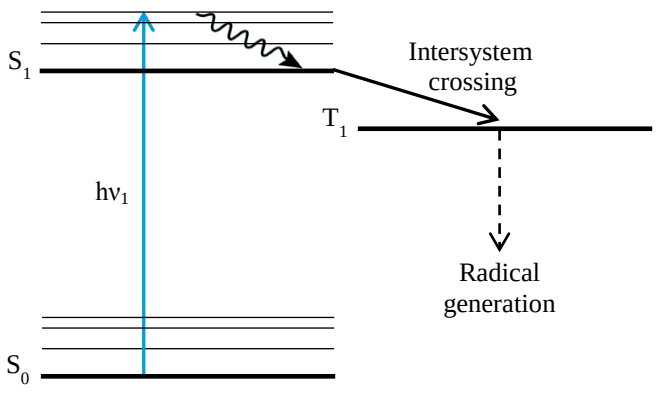

Figure 7: Mechanism of PI excitation from the ground state (S_0) to an excited state (S_1) through a single-photon absorption and radical formation from the triplet state (T_1).

1PP provides a simple and cost-effective fabrication technique for well-known applications such as UV-photolithography and stereolithography. This method has been mostly used to conduct the polymerization at or near the surface of a photosensitive resin to fabricate 1D or 2D structures. A high-frequency beam such as UV is largely absorbed to the resin; hence, it polymerizes the exposed sample from the surface. This results in the attenuation of the beam intensity and distortion of the localized spot within the resin. [85, 87] Therefore, 1PP is mostly a planar process limited to the surface of the sample as illustrated in Figure 8.a. [85]

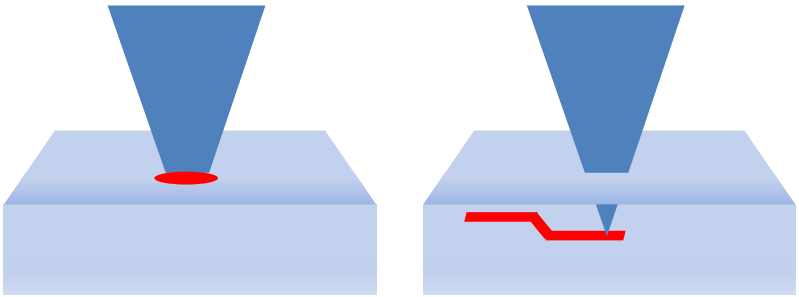

Figure 8: A simple illustration of incident beam penetration in a photosensitive resin. In the case of single-photon polymerization (a) light is absorbed by the surface molecules and cannot penetrate within the resin. In two-photon polymerization (b), penetration of the beam inside the sample results in the fabrication of 3D structures.

Although 3D patterning is not possible by conventional methods of 1PP using UV sources, Maruo and Ikuta reported the fabrication of 3D microstructures using a continuous wave (CW) blue laser [88, 89]. According to their results, by tightly focusing the laser spot on a photopolymerizable resin, localized polymerization based on the nonlinear response of the resin to the optical density is achievable. The photoabsorption at the utilized wavelength has to be adequately small in order to perform the pinpoint solidification in a deep region of the resin. [88] Nonlinear response of the photopolymerization is due to the absorption of highly reactive oxygen molecules by the resin. Oxygen molecules sweep the radicals and prevent them from initiating the polymerization. Hence, if the intensity of incident light is not high enough, the polymerization does not propagate since oxygen molecules consume almost all of the photons. Therefore, by focusing and adjusting the intensity of the light, one can benefit from this phenomenon and solidify desired parts of the resin selectively. [88, 90] By accurately focusing the blue laser beam to the resin and optimizing the exposure, the intensity is enough to perform polymerization in the vicinity of the beam focus but not at the surrounding regions [90, 89]. Then, by scanning the beam inside the resin, the pinpoint solidification of desired spots and fabrication of 3D microstructures through 1PP is achievable [88].

Another method that has been vastly used for 3D microfabrication to improve the spatial resolution in three dimensions is two-photon initiated polymerization [88]. The principle of two-photon polymerization is described in the next section.

4.3 Two-photon photopolymerization

Two-photon polymerization (2PP) is a localized nonlinear polymerization process which is used to fabricate polymeric micro/nanostructures by focusing a near-infrared (NIR) laser beam into photoresists. In this fabrication method, the resin is polymerized by simultaneous absorption of two photons with almost double wavelength than that used in 1PP. [72, 91] Two-photon absorption (TPA) was experimentally discovered in 1961 by Kaiser and Garrett though it was theoretically predicted as early as 1931 [92]. For years, it was only used for spectroscopical purposes until its usage for polymerization induction was reported in 1965 by Pao and Rentzepis [93]. The method was further developed as a tool for lithographic microfabrication by Kawata's group in 1997 [94]. In 1990s, the commercialization of femtosecond lasers in addition to recognition of high-efficiency PIs significantly accelerated the micro/nanofabrication in solid and liquid media through 2PP. Properties such as ultrashort pulse duration (less than 5 fs), high beam quality, coherence, substantial nonlinearity, power and frequency stability, high transient power, and strong localization of femtosecond lasers, have enabled controllable processing of variety of materials by these lasers. [72, 91] Since then, this direct laser writing (DLW) technique has been widely applied to fabricate various photonic, micro-optical, and microchemical components [72].

The principle of TPA is based on the nonlinear response of two-photon transition rate to the optical intensity [88]. PIs in the ground state (S_0) are excited to an excited state (S_1) by simultaneously absorbing two photons, followed by nonradiative relaxations and radical formation. If the energies of two photons are exactly of the same amount, this process is called degenerate TPA otherwise it is a non-degenerate one. In the case of degenerate TPA, equations (16) and (17) can be re-written as:

$$PI \xrightarrow{2h\nu_2} PI^* \rightarrow R\cdot \tag{21}$$

$$PS \xrightarrow{2h\nu_2} PS^* \cdots \xrightarrow{PI} PI^* \rightarrow R\cdot \ , \tag{22}$$

where $\nu_2 \sim \nu_1/2$ is the photon frequency in two-photon excitation process. To make the case clear, it can be assumed that when the first photon is absorbed by the molecule, a virtual intermediate state is created. The lifetime of the virtual state is as short as several femtoseconds. If the second photon irradiates the molecule before decaying of the virtual state, TPA happens successfully. This mechanism is called simultaneous TPA. In addition to simultaneous TPA, there is another mechanism of absorption which is called stepwise absorption. The requirement for stepwise absorption is the existence of a real intermediate energy state. First, a population of electrons from the ground state (S_0) is excited to an actual intermediate state (S_1) through absorption of the first photon. Then,

the excited population will be further pumped to the final level (S_2) by absorbing another photon with usually the same energy of the first one. This process can be considered as two sequential single-photon absorptions. [72] A schematic drawing to show the difference between stepwise and simultaneous TPA mechanism is presented in Figure 9.

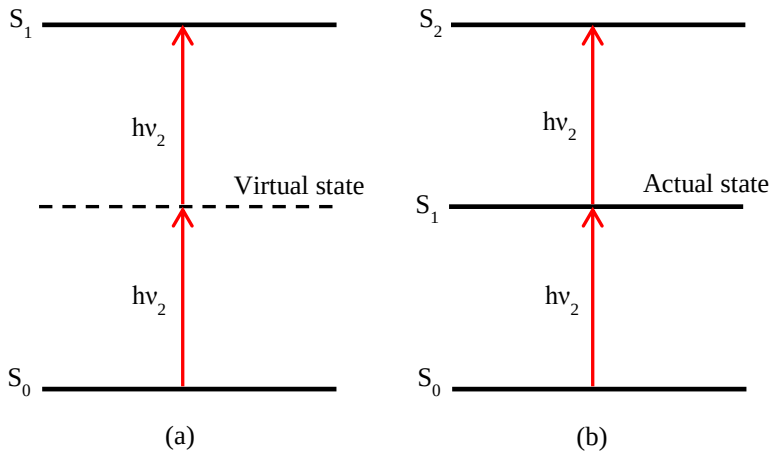

Figure 9: Schematic of (a) simultaneous TPA with a virtual intermediate energy level and (b) stepwise TPA with an actual intermediate energy level.

In a nonlinear optical process such as TPA, the imaginary part of the nonlinear susceptibility is responsible for the energy transfer from the light beam to the medium. The energy change through light-matter interaction per unit time, per unit volume is

$$\frac{dW}{dt} = \langle \vec{E}.\vec{P} \rangle , \tag{23}$$

where $\vec{E}$ is the electric field vector, $\vec{P}$ is the material polarization vector, and brackets define the average over time. The relation between electric field and polarization is

$$P = \chi^{(1)}E + \chi^{(2)}E^2 + \chi^{(3)}E^3 + \cdots, \tag{24}$$

where $\chi^{(1)}$, $\chi^{(2)}$, and $\chi^{(3)}$ refer to linear, second-order and third-order susceptibilities, respectively. Susceptibilities with even orders like $\chi^{(2)}$ do not contribute to resonance processes while imaginary part of $\chi^{(3)}$ plays a major role in nonlinear TPA. In the case of degenerate absorption of photons, the energy transfer rate is

$$\frac{dW}{dt} = \frac{8\pi^2\omega}{c^2n^2} I^2 \mathrm{Im}\left[\chi^{(3)}\right], \tag{25}$$

in which, ω is the angular frequency, n is the refractive index of the medium, and I is the light intensity. The equation shows the quadratic dependence of the TPA rate on the

light intensity that results in improvement of 3D spatial resolution with better accuracy than that in conventional single-photon processes. [72]

Most of the resins that are polymerized by UV or visible light exposure in 1PP can undergo the same reactions when absorbing two photons in 2PP procedure. The only requirement in the case of 2PP is that the light intensity has to be sufficiently high. Utilizing pulsed laser technology, it is possible to enhance the energy of a single pulse to more than four orders of magnitude making the polymerization threshold of any kind of resin accessible. For instance, the energy of an individual pulse in a Ti: Sapphire laser amplifier is 1mJ, which is sufficient to polymerize any UV-polymerizable resin. However, features such as usability, TPA efficiency, tolerance to variation of exposure dose, and laser-induced breakdown are still material dependence factors. [72]

A determinant factor in TPA efficiency, is the absorption cross-section δ which describes the capability of the sample material to absorb photons, and is defined by

$$\delta = \frac{8\pi^2 h\nu^2}{c^2 n^2 N} I^2 \mathrm{Im}\left[\chi^{(3)}\right], \tag{26}$$

where N is the number density of absorbing molecules [72]. Another important parameter, which effects on TPA efficiency, is the fraction of excitations resulting in polymer initiation Φ_0. In order to obtain efficient absorption and initiation, δ and Φ_0 need to be high enough. This condition can be met by choosing high-efficiency PIs and radical based polymerization mechanisms. Radical based processes amplify the photo-induced procedure by adding lots of monomers to the polymer chain in every single initiation event. [95]

Process of 2PP occurs in a minuscule 3D volume at the focal point, less than the cubic wavelength (λ^3). That leads to a unique advantage of 2PP that is high 3D resolution in polymer resins (Figure 8.b). Another benefit is that the excitation process is a heat insulating process where the photon energy deposition is so fast that there is not enough time for electrons to consume it for phonon emissions. This feature is valuable in photochemical and photophysical reactions where non-localized thermal effects are undesirable. In addition, polymers usually exhibit negligible linear absorption in red-NIR regime. It allows the laser beam to penetrate deeply into the sample and directly induce the polymerization inside the material without disturbing outside of the focal volume. All of these features make 2PP a beneficial tool for various applications. [72] However, since TPA has extremely small transition probability, using a short-pulsed laser source such as Ti: Sapphire is essential, and these sources are usually expensive compared to conventional CW sources which are used in 1PP. Therefore, microfabrication through 1PP, using CW lasers with a spatial resolution comparable to that of 2PP can be more cost-effective for many purposes. [88]

5. METHODOLOGY

In this chapter, the experimental methods of fabrication, imaging, and optical characterization of fluorescent microstructures containing silver NCs in PVA films are explained. The process of sample preparation in clean room is described in detail. This is followed by the illustration of custom built setups of direct laser writing (DLW), bright field microscopy, fluorescence microscopy, and fluorescence spectroscopy of the microstructures. Finally, the method of atomic force microscopy (AFM) to obtain the thickness of polymer films and topography of the written structures is presented.

In this thesis, samples were prepared in a clean room located at Optoelectronic Research Center (ORC) of Tampere University of Technology (TUT). The procedure of DLW, fluorescent spectroscopy and microscopy was conducted at the Optics Laboratory of the Department of Physics of TUT. All the AFM measurements and imaging were performed at Aalto University Nanomicroscopy Center (Aalto-NMC).

5.1 Sample processing

The first step in sample preparation was cleaning the substrates. The substrates used in the experiments were 170-200 μm thick cover-glasses with 25 mm diameter manufactured by Electron Microscopy Sciences (EMS). First, the glass coverslips were wiped by acetone-saturated clothes. To remove the deposited layer of acetone on coverslips, they were further cleaned by ethanol. Finally, the glass coverslips were rinsed with Milli-Q (MQ) water with resistivity of 18.2 MΩ.cm and dried with Nitrogen.

Thin films of PVA containing silver (Ag@PVA) were prepared by spin-coating aqueous Ag@PVA solutions with different concentrations of silver. The raw polymer material used in this work was 99% hydrolyzed PVA powder manufactured by Sigma-Aldrich, and its molecular weight varied between 89000 to 98000 g/mol. To perform the calculations, we considered a mean value of molecular weight of PVA that is 93500 g/mol. 3 wt% of PVA aqueous solution was prepared by dissolving 240 mg of PVA powder in 8 ml of MQ water. In order to dissolve PVA with a large degree of hydrolysis (99%) in water, the liquid was stirred and heated up to 70° C. Simultaneously, the amounts of 50 mg, 75 mg, 100 mg, 125 mg, and 150 mg of silver nitrate ($AgNO_3$) powder (169.87 g/mol, Sigma-Aldrich) were weighted and each was dissolved in 8 ml of MQ water. Then, each one of the aqueous solutions of $AgNO_3$ was mixed with a 3 wt% PVA solution. Eventually, the final Ag: PVA ratios of 21 wt%, 31 wt%, 42 wt%, 52 wt%, and 62 wt% were obtained. One PVA solution without mixing

with $AgNO_3$ was also prepared to ensure that the fluorescence is only originated from the silver NCs.

The programmable spin coater (OPTIcoat ST 22+, ATMsse) was used to prepare polymer films from the solutions. First, the spinner was initialized. Then, a clean glass cover slip was placed on the center of a circular sample holder plate in such a way that the substrate covered a small vacuum hole in the center of the plate. A regular syringe was used to pour 500 µl of the Ag@PVA solution on the surface of the substrate. In order to prevent the formation of air bubbles in the film, the syringe mouth was kept as close as possible to the substrate without touching it. The spin-coating speed of 1500 rpm, and time of the closed bowl spinning of 120 s were selected from the programs list on the spin coater. Vacuum was applied to the substrate to keep it constant during spin-coating. After completion of the spin-coating, the sample was lifted carefully; then, it was placed inside the nitrogen desiccator cabinet for 12 h to be dried. Care was taken to minimize the exposure of the ambient light to the sample.

After drying the sample for 12 h in the desiccator, it was mounted on a clean microscopy slide, using picodent temporary glue, to be prepared for DLW. This completed the sample preparation process and the sample was placed on a sample holder of DLW setup for laser exposure.

5.2 Direct laser writing setup

The main components of DLW system are laser source, beam delivery setup, and specimen mounting components [12]. In this work, a custom-built 1PP setup as shown in Figure 10 was used to write desired 2D microstructures in Ag@PVA films. A tunable continuous-wave (CW) single mode diode laser (DL 100, TOPTICA Photonics) was used as a laser writing source. In all the DLW experiments, we used laser beam of wavelength 405 nm. The laser power was controlled by a polarizer in front of the laser source. We performed the DLW with various writing powers in the range of 50-2000 µW. A combination of two achromatic doublet lenses with focal lengths of 40 mm and 150 mm was set to collimate the beam and increase its diameter. Between two lenses of the collimator, a 25 µm pinhole aperture was used to spatially filter the beam. A spatial filter can provide a clean Gaussian beam with smooth intensity profile by removing the unwanted high-spatial frequencies of the diffraction pattern and allowing low spatial frequencies to pass. It can also decrease the additional spatial noises from the beam. Figure 11 illustrates the combination of a collimator and a pinhole to obtain a collimated Gaussian beam. We fixed the pinhole on a 30 mm XY translating lens mount (CXY1, Thorlabs) and adjusted its position precisely at the focal point of the collimator lenses. An optical beam shutter (SH05, Thorlabs) was placed after the collimator, and it was controlled by a shutter controller (SC10, Thorlabs). The shutter can operate in different modes; single, auto, manual, external gate (x gate), and repeat (REP) modes. In our experiment, we externally provided voltage to control the opening and closure of the shutter in x gate mode by using DAQx card (NI-6363) and

LabVIEW program. A longpass dichroic filter (FF484-FDi01, Semrock) that transmits wavelengths longer than 484 nm and reflects wavelengths shorter than that, was placed at 45 degree angle. As we used 405 nm laser beam for DLW, the beam was reflected towards a 100x, 1.4 NA, oil immersion objective lens (HCX PL APO, Leica). The objective lens focused the laser beam into the sample, which was mounted in the three-axis motorized scanning stage (Nanomax, Thorlabs). The diameter of the focused writing laser spot was around 147 nm calculated by the formula, spot size = $0.51 \times \lambda_{DLW}/NA$. Here, λ_{DLW} is the wavelength of the writing laser beam and was 405 nm in our case. The calculated diameter is the theoretical minimum value of the laser spot if everything is perfect in the setup. In reality, the laser spot might be in order of 200-250 nm. The 2D structures were written by scanning the sample over the fixed laser beam with the scanning speed of 5μm/s. The scanning of the sample stage was controlled by a piezo controller (BPC203, Thorlabs). The piezo controller has three channels to control the movement of stage in three dimensions, and can operate in closed or open loop modes. For all the 2D fabrications, two channels of the piezo controller were used in the closed-loop mode. A data acquisition card (X series DAQ, NI USB-6363) was utilized to input analog signals to the piezo controller through BNC cables. The output analog signal from the DAQx card was controlled using a custom-built LabVIEW code.

In-situ imaging of the DLW process was done with a bright field microscope arm incorporated in the DLW setup. A red light source was adjusted above the sample for bright-field microscopy. The scattered light from the sample was collected by the objective lens and transmitted through the dichroic mirror. A 200 mm achromatic doublet lens was located after the dichroic mirror to focus the light on a CMOS camera (DCC145M, Thorlabs), or an electron multiplying charge coupled device (EMCCD) camera (iXon3 897, Andor). A filter (BLP01-488R-25, Semrock) was used before the camera to prevent transmitting the reflected laser light into the camera.

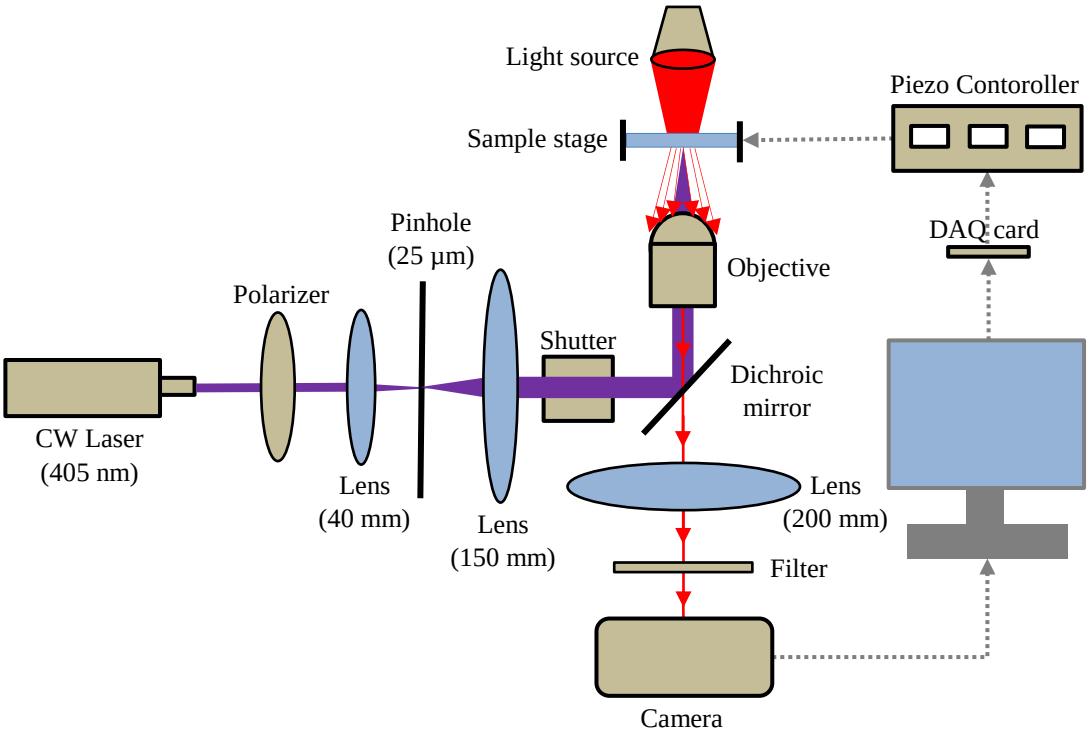

Figure 10: Schematic diagram of a custom-built DLW setup to fabricate 2D fluorescent microstructure in Ag@PVA films using 1PP process.

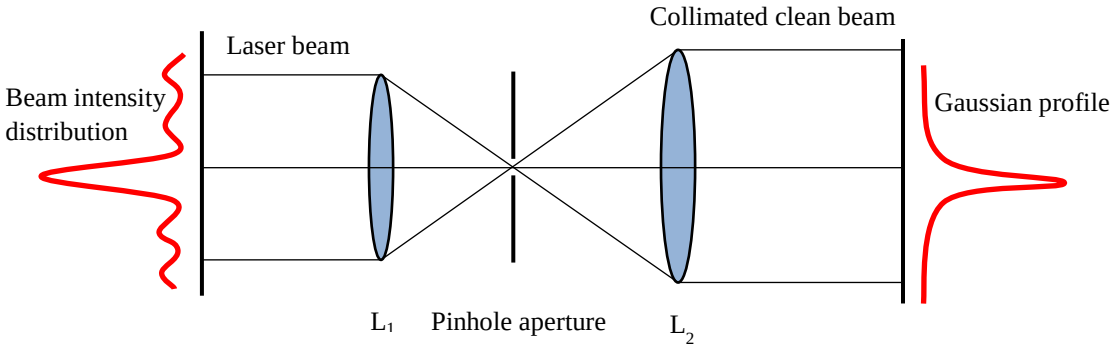

Figure 11: Illustration of a collimator consisting two doublet lenses, L_1 and L_2, and a pinhole aperture. The beam is spatially cleaned and its diameter is increased after passing through this collimation system.

5.3 Fluorescence microscopy

The schematic diagram of a custom-built fluorescence microscopy setup is shown in Figure 12. In order to record the images from the fluorescent microstructures, 470 nm light emitting diode (LED) (Osram) was used as an excitation source. An excitation filter (FF02-470/100, Semrock) was placed after the LED. This band pass filter allows passing light of wavelength from 420 nm to 520 nm and blocked the unwanted leakage of LED light. An achromatic doublet lens (f = 100 mm) was used to focus the LED light

to the back aperture of the 100 x objective lens (HCX PL APO, Leica). The dichroic mirror (FF484-Fdi01, Semrock) was placed at 45 degree that reflected LED light towards the objective lens. The objective lens defocused the LED light illuminating the larger circular area with diameter of around 45 μm. After illuminating the written structure with 470 nm LED light, the fluorescence emitted from the structure was collected by the objective lens. It was then directed to the dichroic mirror, and focused on the EMCCD camera through a 200 mm tube lens located after the dichroic. An emission filter (BLP01-532R-25, Semrock) was placed in front of the camera to block any remnant excitation light. A bright field microscope was also incorporated in the setup to locate the written structure prior to fluorescence imaging. The recorded images were then processed and colored according to the gray scale intensity values by using by using ImageJ software.

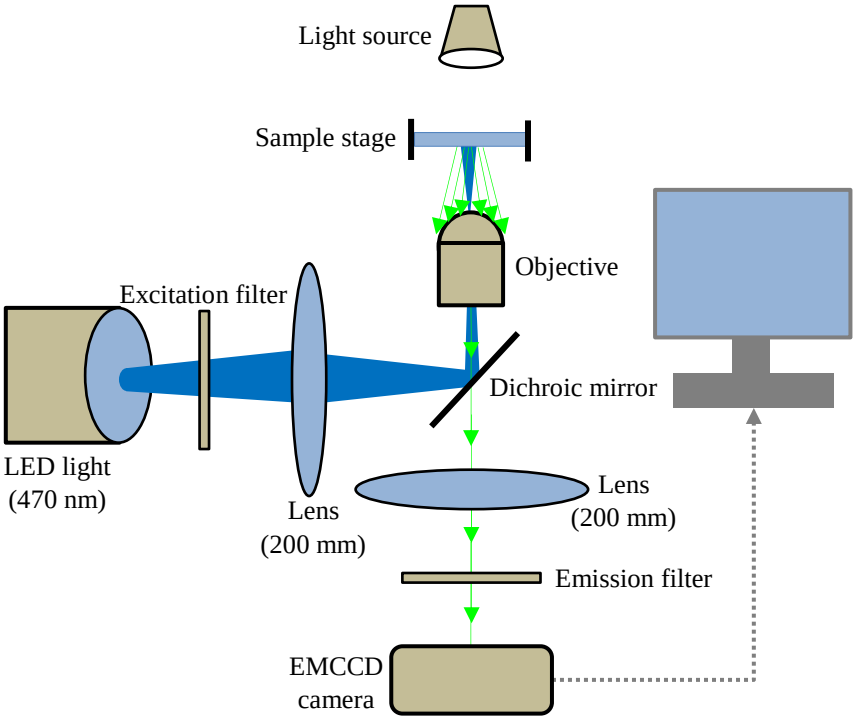

Figure 12: Schematic diagram of a custom-built fluorescence microscopy for imaging the 2D fluorescent microstructures in Ag@PVA film.

5.4 Fluorescence spectroscopy

We carried out spectroscopy experiments to investigate the formation of silver NCs and study their optical properties. We also studied the effects of determinant parameters such as the concentration of silver and laser writing power on the fluorescent intensity of microstructures. In addition, the photostability of the NCs was studied by recording the fluorescence spectra when continuously irradiating the written structures with light.

The custom-built fluorescence spectroscopy setup is illustrated in Figure 13. This setup consists of a 473 nm laser diode (MLD series, Cobolt) as an excitation source. In

order to control the excitation power, a polarizer was located in front of the laser source. For different experiments, we used different excitation powers in the range of 1-10 mW. A collimator-pinhole system including two achromatic doublet lenses with focal lengths of 30 mm and 200 mm and a 25 μm pinhole aperture was set after the polarizer spatially clean the beam and increase its diameter. The shutter (SH05, Thorlabs), controlled by the controller (SC10, Thorlabs), was located in front of the collimator to govern the excitation time. The collimated beam after passing the shutter was directed to a dichroic mirror (FF484-Fdi01, Semrock).The reflected light from the dichroic filter was directed towards the 100 x oil immersion objective lens with 1.4 NA (HCX PL APO, Leica). Before the dichroic mirror, an achromatic doublet lens (f = 200 mm) was used to focus the beam onto the back aperture of the objective. Then, the microscope objective defocused the beam to illuminate a larger circular area with diameter of around 45 μm on the sample. The emitted fluorescence from the structure was collected by the objective lens and passed through the dichroic mirror. Afterward, it was focused to a fiber-optic spectrometer (Avac-pec 2048, Avantes) through a 40 mm achromatic doublet lens. In front of the spectrometer, an emission filter (BLP01-488R-25, Semrock) was placed to block the remnant excitation light. Before starting the measurements, we had to find the location of a set of the written line-array structures in the sample. To find the microstructures we used a bright field microscopy arm equipped with EMCCD camera similar to that in the DLW setup. In case of bright field imaging, the sample was illuminated with the red light source, and the scattered light was directed to the EMCCD camera by the flip mirror. This flip mirror, placed between the spectrometer and a 200 mm tube lens, guided the light either to camera or spectrometer. The sample was illuminated with the red light source, and the scattered light was guided to the EMCCD camera by the flip mirror for bright field microscopy. Using this optical fluorescence spectroscopy setup we performed different experiments, which are given below:

Concentration test. In order to perform this test, we prepared samples with different Ag: PVA ratios of 21 wt%, 31 wt%, 42 wt%, and 52 wt%. DLW with 405 nm laser diode was performed to write the line pairs with spacing of 1 μm in all of the samples. Laser writing intensity was set to 59 GW/m^2, and scanning speed was fixed to 5 μm/s. The fluorescent spectra were recorded with similar condition (excitation laser wavelength = 473 nm, excitation laser intensity = 3 MW/m^2, and integration time = 500 ms). The recorded spectra were studied very carefully and presented in results and discussion.

Different power writing test. In this test we fabricated line arrays with 1 μm line spacing in 52 wt% sample with different laser writing intensities of 15 GW/m^2, 29 GW/m^2, 41 GW/m^2, 59 GW/m^2, and 88 GW/m^2 at constant scanning speed of 5 μm/s. We recorded the fluorescent spectra from each structure at similar excitation condition (excitation laser wavelength = 473 nm, excitation laser intensity = 3 MW/m^2, integration time = 500 ms).

Photostability (Bleaching) test. The fluorescence-bleaching test was also perforems using the same optical setup. In this experiment, we studied the fluorescence

bleaching using different excitation laser wavelengths. Hence, we used a 532 nm single-frequency CW laser source (Millennia Pro, Spectra Physics) in addition to the 473 nm laser diode, as another excitation source. When using 532 nm excitation source, the emission filter was also changed to the long pass filter (BLP01-532R-25, Semrock). Emission spectra were recorded continuously for 5 min from the area containing the written structure as well as area unexposed to the writing beam (considered background) by exciting the areas with laser intensities of 0.6 MW/m^2, 3 MW/m^2, and 6 MW/m^2, and laser wavelengths of 532 nm and 473 nm. In this measurement, integration time was set to 1 s and 300 sets of data were recorded from one structure. For all the measurements, the small signal from glass emission under the same excitation condition was subtracted. The fluorescence intensities, which were obtained by integrating the area under emission curves, were plotted against the time.

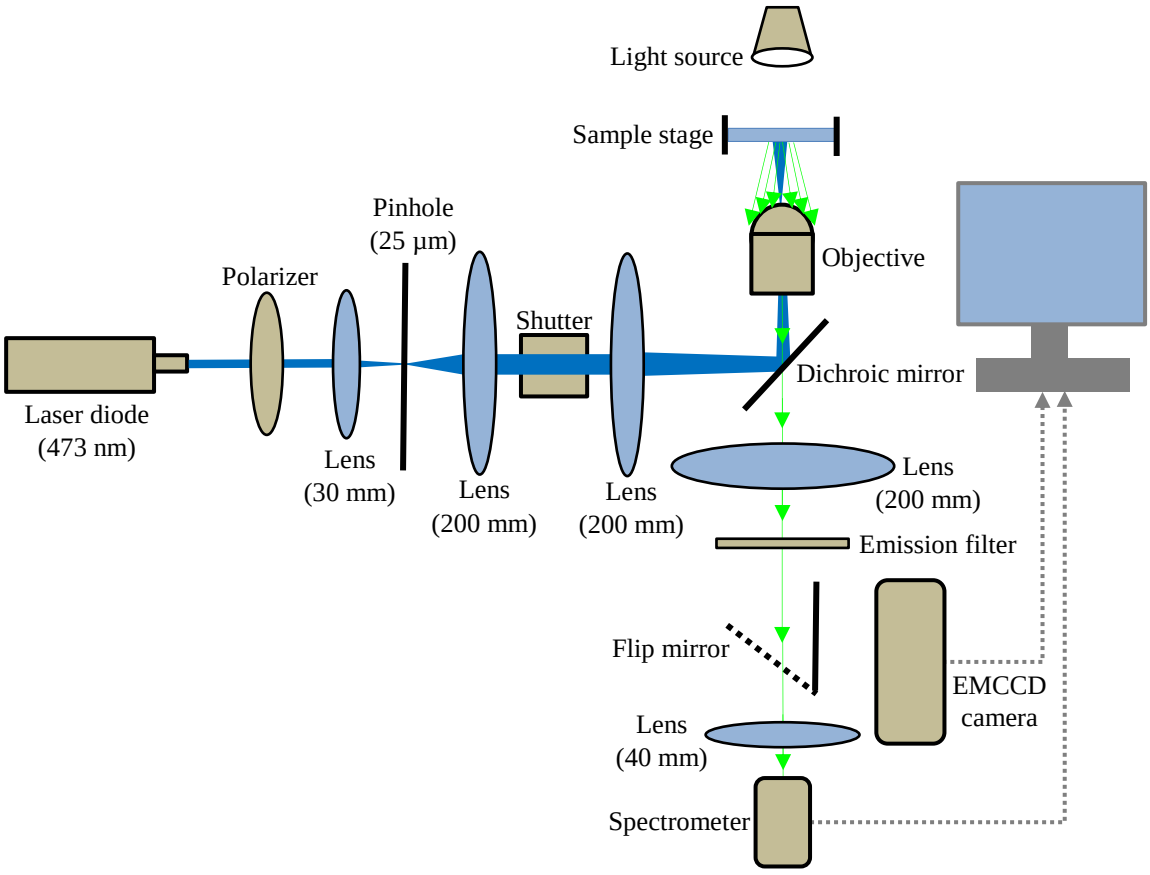

Figure 13: Schematic diagram of a custom built fluorescence spectroscopy setup for optical characterizations of 2D fluorescent microstructure o Ag@PVA films.

5.5 Atomic force microscopy

Atomic force microscope (AFM) was used to determine the thickness of Ag@PVA films and topographical features of the written structures. Sample with silver concentration of 42 wt% in PVA was used for the AFM studies. Line arrays with 2 µm line spacing were written with laser intensities of 59, 88, and 117 GW/m^2 and with constant scanning speed of 5 µm/s. The AFM measurements were performed by using

the AFM (Dimension 5000, Veeco) in tapping mode. Since the samples were soft, it was important to use AFM in tapping mode, which is less destructive than contact mode AFM. In the tapping mode, the tip touches the surface for a short time to avoid the problems of high lateral tip-sample forces in contact mode. The system contains an XYZ open loop scanning head to measure the desired features in three dimensions, and a NanoScope V controller, which enables recording the tip-sample interactions to probe nanoscale events. In order to obtain the topographical characteristics of the structures, the AFM probe tip (HQ: NSC15/Al BS, MikroMasch) was brought into the proximity of the sample. The probe and the specimen were moved relatively to each other in a raster pattern. The interactions between the sample surface and the tip were measured by monitoring the displacement of the free end of a cantilever, which was attached to the probe tip. In order to measure the film thickness, the film was scratched with a scalpel and then, the AFM tip was scanned perpendicular to the scratch, and the tip-sample interactions were recorded. The AFM images were further processed and analyzed by Gwyddion software to determine the film thickness and topographical characteristics.

6. RESULTS

In this thesis work, several experiments were performed to fabricate and characterize fluorescent microstructures containing silver NCs. The results obtained from the experiments are presented in this chapter. At first, the outcome of AFM measurement of the polymer film thickness is presented. Then, the images and AFM data obtained from the written structures are illustrated. Afterward, the effects of silver concentration and writing laser power on the fluorescence intensity are discussed, which is followed by the results acquired from several bleaching experiments.

6.1 Polymer film analysis

In order to characterize the laser-written structures, we first needed to investigate the thickness of Ag@PVA film that was spin coated on a glass cover slip. For this purpose, a scalpel scratch was made on the 42 wt % Ag@PVA layer, and it was imaged by AFM. The AFM image was analyzed and by obtaining the line profile of the scratched region the thickness of the Ag@PVA film was estimated to be 58 nm. Figure 14 indicates the line profile corresponded to the scalpel scratch on the polymer film along with an AFM image of the region containing the scratch. The dark area in the AFM image represents the polymer layer and the lighter area indicates the glass substrate.

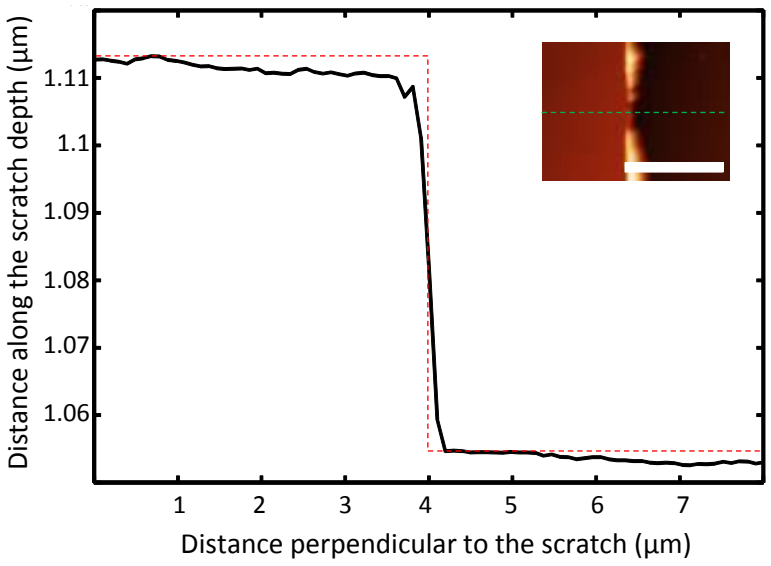

Figure 14: Line-cut topography profile of the Ag@PVA-glass across the dashed line in the AFM image (inset). The distance corresponding to the depth of the scratch is marked by the red vertical dashed line. Length of the scale bar in AFM image is 4 µm.

6.2 Written structures

Figure 15.a illustrates the bright-field image of line arrays fabricated by DLW using 1PP process. The structures are written on 42 wt % Ag@PVA sample. The writing laser wavelength was 405 nm, and laser intensity (I_{dlw}) was fixed to 59 GW/m^2. The scanning speed of 5 µm/s and line spacing of 1 µm were set from LabVIEW program. The fluorescence image (Figure 15.b) was obtained by exciting the written structure with a 473 nm LED light source with the excitation intensity of 1 MW/m^2 considerably lower than I_{dlw}. The fluorescence image has been false-colored by ImageJ program. As Figure 15.b depicts, the written structures exhibit bright fluorescence compared to the regions, which were not exposed to the writing laser beam (background areas). Figure 15.c illustrates the intensity profile of fluorescence across the line array with an average line breadth of 400 nm. The dashed line in Figure 15.b shows the location from which the fluorescence intensity profile has been drawn. The significant difference in fluorescence intensities of written structures and background regions corresponds to the formation and stabilization of silver nanoclusters fabricated through DLW.

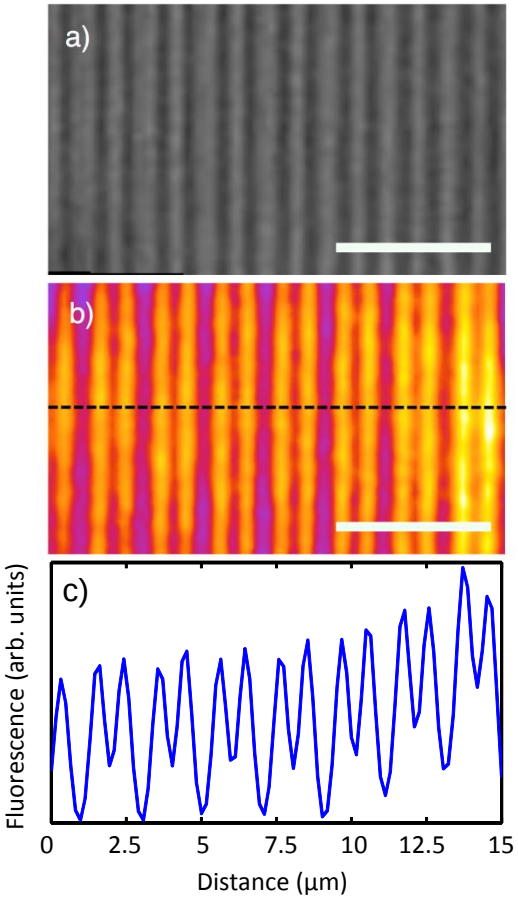

Figure 15: (a) Bright-field microscopy image of a fabricated line array in 42 wt % Ag@PVA sample (I_{dlw} = 59 GW/m^2, λ_{dlw} = 405 nm). Length of the scale bar is 5 µm. (b) Fluorescence image of the same structure (I_{exc} = 1 MW/m^2, λ_{exc}=473 nm). (c) Fluorescence intensity profile across the dashed line in (b).

Moreover, the detailed analysis of the written structures on 42% Ag@PVA samples was performed through AFM characterization. The AFM results indicated the formation of grooves in the exposed areas. Figure 16 shows the AFM images of the structures written with different I_{dlw} and the corresponding line profiles along the marked regions. The represented line profiles are the results of averaging over 15 profiles obtained from each AFM image. The depths in line profiles manifest the formation of 3D grooves at the positions of the laser-written structures. The depths and widths of the grooves were extracted from the profiles, and the mean values were calculated for each structure. The depths of the grooves made by laser intensities of 59 GW/m^2, 88 GW/m^2, and 117 GW/m^2 were measured to be 32 nm, 35 nm, and 38 nm, respectively. The corresponding values of the widths were found to be around 377, 600, and 700 nm, respectively.

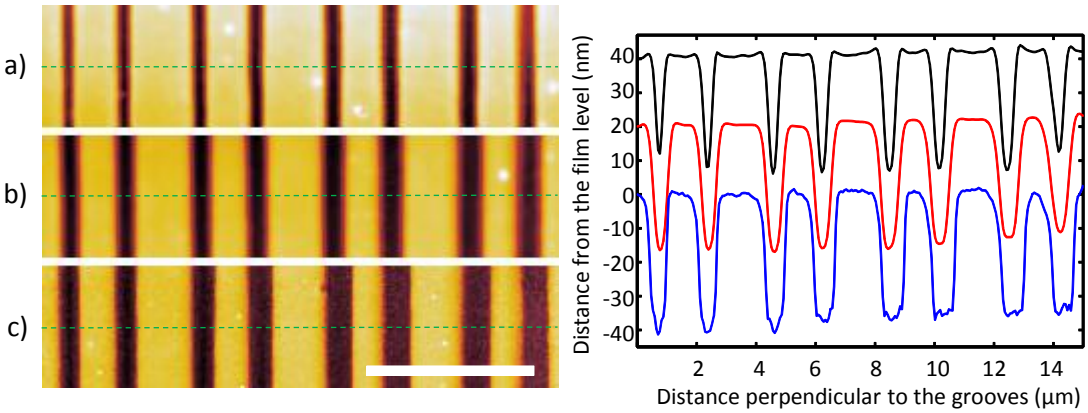

Figure 16: AFM images of the structures written with I_{dlw} of a) 59 GW/m^2, b) 88 GW/m^2, and c) 117 GW/m^2 in 42 wt % Ag@PVA samples (left). Length of the scale bar is 5 µm. Line-cut topography profiles of the structures across the dashed lines (right). For clarity, the line profiles of a) and b) have been vertically shifted by 40 and 20 nm, respectively.

6.3 Effect of silver concentration

To investigate the origin of the fluorescence emitted from the written structures in Ag@PVA films, we performed the DLW experiment on samples with different Ag/PVA weight ratios (0% to 62%). For all the experiments, the writing laser intensity and the scanning speed were fixed to I_{dlw} = 59 GW/m^2, and 5 µm/s respectively. For PVA films without silver, we could not visualize changes caused by this laser intensity or even higher intensities. Therefore, we skipped that sample from further spectroscopy measurements. The fluorescence emission spectra from other samples were recorded by exposing the written structures to the 473 nm laser beam. The excitation power of the laser was set to 3 MW/m^2 and samples were exposed to the beam for 500 ms. The weak fluorescence spectrum emitted from the glass substrate was subtracted from all the measured spectra. The result of the concentration test is illustrated in Figure 17. It indicates that the fluorescence intensity increases with increasing the silver concentration. Dependence of the fluorescence signal on the silver concentration confirms that the fluorescence is due to the silver NCs in PVA films. Moreover, the

observations of the fluorescent structures and intensity profiles obtained from fluorescent images (Figure 15.c) suggest that the fluorescence emission is due to the silver NCs at the depth of the grooves. The structures written on samples with Ag/PVA weight ratio of 62% and more were also fluorescent; however, due to the high concentration of silver we observed some undesired crystallizations. Therefore, the measured results of those samples were not reliable, and they were omitted from the studies.

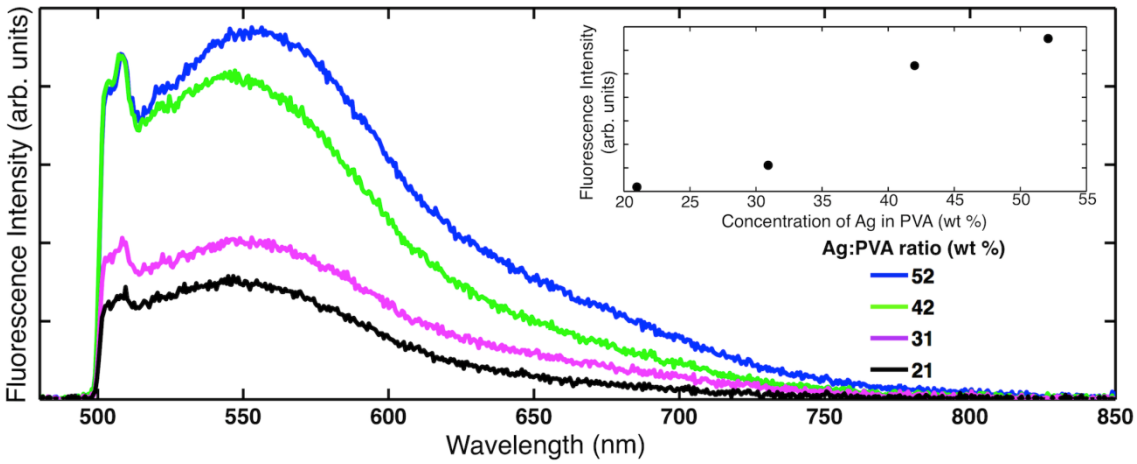

Figure 17: Fluorescence emission spectra of laser-written silver NCs in Ag@PVA films with Ag/PVA weight ratios in the range of 21 to 52% (λ_{exc} = 473 nm). The inset image illustrates the dependence of the fluorescent intensity on Ag concentration.

6.4 Effect of laser writing power

The fluorescence intensity of the written structures varied with changing the laser writing power while all the other parameters such as the silver concentration, and scanning speed kept constant. Figure 18 illustrates the fluorescence emission spectra from the structures written with I_{dlw} in the range of 15 GW/m^2 to 88 GW/m^2. It is clear from the emission spectra that the fluorescence emitted from the structure written by the highest writing power has the maximum intensity. It was possible to write structures by applying lower laser intensities down to 5 GW/m^2 though simultaneously visualizing the DLW process with our bright-field microscopy setup was difficult. Therefore, finding the exact focus of the writing laser in order to write uniform and clear structures for further analysis was not possible. The emission spectra were recorded by exciting the structures through 473 nm laser beam with the intensity of 3 MW/m^2 and exposure time of 500 ms. The fluorescence spectrum of the glass substrate was subtracted from the data.

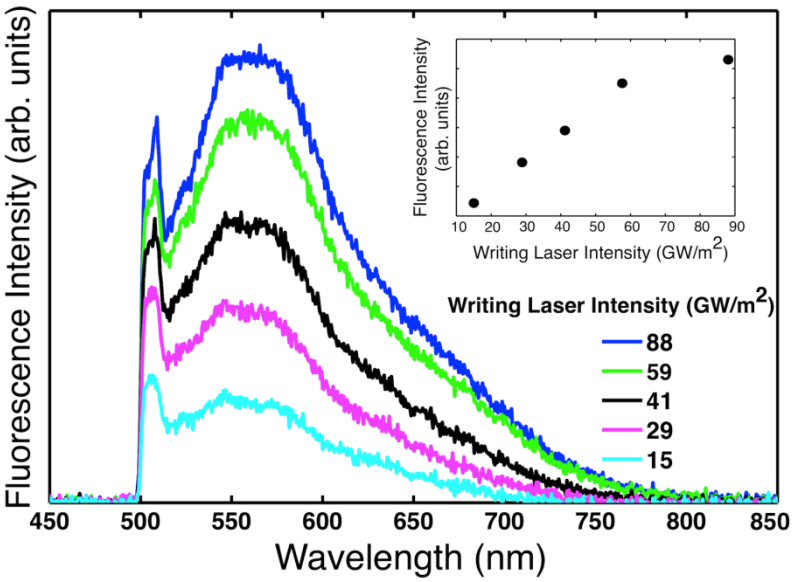

Figure 18: Fluorescence emission spectra (λ_{exc} = 473 nm) of laser-written structure in Ag@PVA film. Writing laser intensity varies from 15 to 88 GW/m^2. The inset image illustrates the dependence of the fluorescent intensity on the writing power.

6.5 Photobleaching of silver nanoclusters

In order to investigate the photo-stability of the fluorescent structures in time, we performed several experiments to study the photobleaching of the silver NCs in detail. Two different areas of the sample were the subjects of these studies. One part was an area containing laser-written structures, and the other one was an area unexposed to the writing beam (background). Microstructures were written with I_{dlw} of 59 GW/m^2 (λ_{dlw} = 405 nm) on 42 wt % Ag@PVA sample. Two different excitation sources with wavelengths of 473 nm and 532 nm, and laser intensities of 0.6 MW/m^2, 3 MW/m^2, and 6 MW/m^2 were utilized to excite the structures and background regions. The chosen regions were continuously exposed to a defocused laser spot for 300 s. The emitted spectrum from the sample was recorded every 1s. Eventually, by integrating the area under each spectrum curve, the total fluorescence intensity was calculated. Figure 19 andFigure 20 depict the normalized bleaching data plotted against time when the sample was irradiated with 473 and 532 nm excitation sources respectively. The weak fluorescence emitted from glass is subtracted from all data. As expected, the results showed that the high fluorescence intensity which was detected at the very first moment of the exposure exponentially decreases with time. Moreover, it can be seen from the curves that the structures bleach faster when the excitation power is increased.

Surprisingly, when the sample was exposed to the 473 nm laser beam, we detected the fluorescence signal also from the background region, which was increasing with time and excitation power. This background signal is attributed to formation of NCs. However, as it is indicated in Figure 20, there was almost no fluorescence signal from the background when the sample was exposed to 532 nm excitation source for 300 s. We believe that the 532 nm laser beam with above mentioned laser intensities is unable to form NCs within 300 s of exposure.

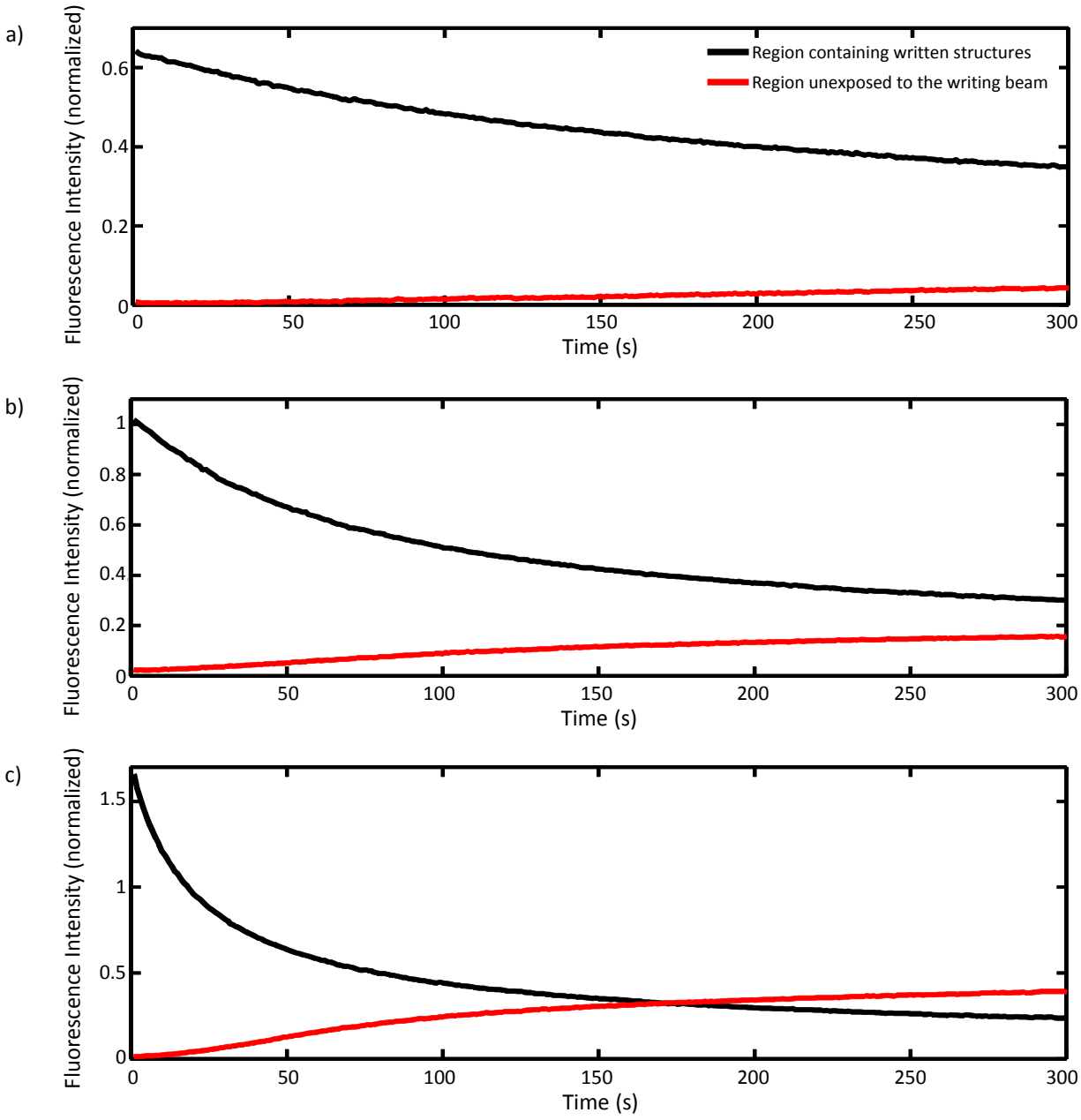

Figure 19: Total fluorescence intensity detected from the area containing laser written structures (black curve), and area unexposed to the writing beam (red curve) during 300 s time interval. The structures were written with I_{dlw} of 59 GW/m^2 (λ_{dlw} = 405 nm) in 42 wt % Ag@PVA film. The fluorescence signals were obtained by irradiating the sample with 473 nm excitation source and I_{exc} of (a) 0.6 MW/m^2, (b) 3 MW/m^2, and (c) 6 MW/m^2.

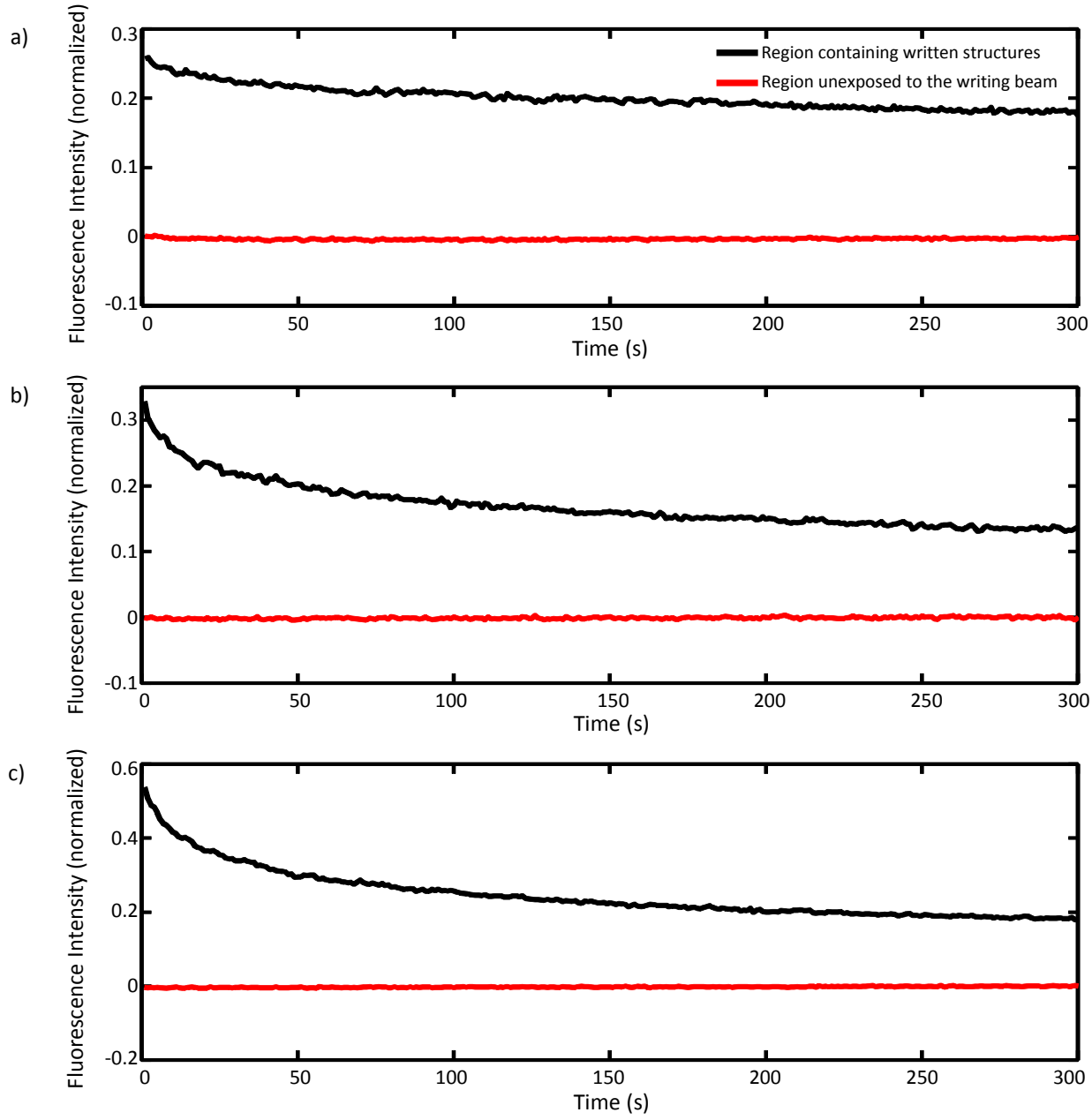

Figure 20: Total fluorescence intensity detected from the area containing laser written structures (black curve), and area unexposed to the writing beam (red curve) during 300 s time interval. The structures were written with I_{dlw} of 59 GW/m^2 (λ_{dlw} = 405 nm) in 42 wt % Ag@PVA film. The fluorescence signals were obtained by irradiating the sample with 532 nm excitation source and I_{exc} of (a) 0.6 MW/m^2, (b) 3 MW/m^2, and (c) 6 MW/m^2.

7. DISCUSSION AND ANALYSIS

Some of the results presented in the previous chapter demand further analysis and clarification. Therefore, the aim of this chapter is to discuss more those outcomes. At first, the formation of the grooves indicated in AFM results is further analyzed. Then, we talk more about the observations from recorded fluorescence emission spectra. Finally, the results of bleaching tests and photostability of the written structures are studied.

7.1 Material ablation

AFM images of the microstructures written with three different laser intensities (I_{dlw} = 59 GW/m^2, 88 GW/m^2, and 117 GW/m^2) along with the corresponding line profiles are presented in Figure 16. Based on the obtained line profiles, the depths of the grooves were measured to be from 32 nm to 38 nm. Moreover, from AFM analysis we calculated that Ag@PVA film thickness was around 58 nm (Figure 14). Comparing the values obtained for the depth of the grooves created through DLW and the film thickness suggests that the DLW process ablates a considerable amount of the materials in the exposed areas. Moreover, the sharp edges of the grooves indicated in the topographic profiles of the structures (Figure 16) imply the lowest aggregation of the materials at the depth of the grooves. However, the fluorescence signal was detected exactly from the regions exposed to the writing laser beam (Figure 15). These results strongly suggest the presence of the silver NCs in the grooves despite the extensive material ablation. Furthermore, despite the fact that the fluorescence was observed from the entire breadth of the grooves, the maximum intensity always corresponded to the middle part of the written lines. Therefore, it can be concluded that the fluorescence signal emanates from the silver NCs at the depth of the structures where there is the minimum agglomeration of other materials. Thus, the fact that silver NCs are the only origin of the fluorescence emission was also confirmed by AFM characterizations.

Kunwar et al. have found similar results while studying 2D direct laser written structures in Ag@PMMA films [5]. In addition to fluorescence and AFM analysis, they performed scanning electron microscopy (SEM)-energy dispersive x-ray spectroscopy (EDS) experiments on the written structures to verify the presence of Ag at the depth of the grooves. Their results not only confirm the presence of Ag in the areas containing written structures, but also they show that the amount of Ag remains constant in both exposed and unexposed regions. Our results are also consistent with the findings of Bellec et al. from the 3D fluorescent nanostructures fabricated through DLW

in silver-containing glass [8]. Their AFM and high-resolution scanning electron microscopy (HRSEM) outcomes also confirm that the maximum intensity of the fluorescence corresponds to the bottom of their written structures where there is a considerable chemical contrast between Ag and other elements.

7.2 Enhanced Raman scattering effect

As discussed in chapter 2.3, in addition to the bright fluorescence, silver NCs exhibit a significant enhancement of Raman scattering signals. Our obtained fluorescence emission spectra depict that the microstructures when excited with 473 nm laser source, exhibit broadband fluorescence emission from 500 nm to 800 nm with an emission maximum peak at around 560 nm (Figure 21). The cutoff of the spectra at wavelengths shorter than 500 nm is due to using the emission filter in order to block the excitation beam. Moreover, it can be observed in the spectra that a narrow sharp peak has been detected at around 510 nm. By comparing the shape of the spectrum and the wavelength in which this sharp peak has been observed with the findings of other studies [5, 96], it can be concluded that most likely this peak corresponds to a Raman enhanced scattering effect. Similar sharp peak has been observed in the emission spectra acquired by Kunwar et al. [5] and Zheng et al. [96] from the fluorescent silver NCs. In the former research, they have conducted Raman spectroscopy and microscopy experiments on laser-written structures in Ag@PMAA films to ensure that Raman scattering is the origin of the observed sharp peak. The detected Raman spectrum and image indicate highly localized Raman signals from the written structures containing silver NCs. The Raman spectrum recorded from their written structures is shown in Figure 22.a. Two broad peaks at 1340 cm^{-1} and 1590 cm^{-1} can be seen in the spectrum while there is no signal detected from unexposed areas. Figure 22.b illustrates the emission fluorescence signals obtained from our written structures in Ag@PVA films excited with 473 nm and 532 nm laser beams (in both cases I_{exc} = 3 MW/m^2). The intensities are plotted against the raman shift (cm^{-1}) from the excitation light sources. The Raman shifts of the sharp peak in both spectra (Figure 22.b) overlap at 1300 cm^{-1} to 1700 cm^{-1}, which is consistent with results shown by Kunwar et al. Our result is also consistent with the outcome of the latter mentioned research where they have detected similar Raman signal from the glycine-coated 3nm silver NPs. We believe the origin of the observed Raman enhanced scattering effect from the silver NCs in our experiments is due to strong interactions of NCs with the surrounding polymer molecules in a charge-transfer process [97].

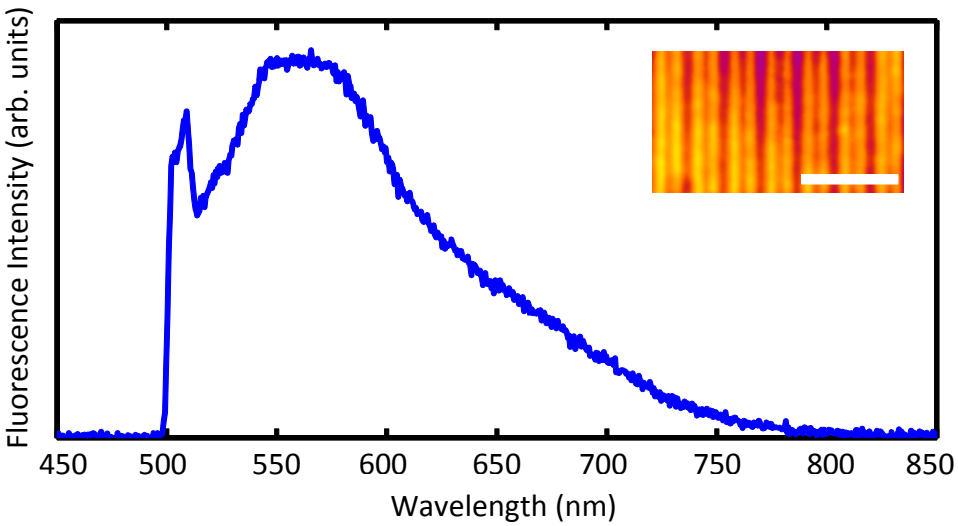

Figure 21: Emission spectrum (λ_{exc} = 473 nm) obtained from fluorescent microstructures. Inset image illustrates the fluorescence image of the written structures. Length of the scale bar is 5 μm.

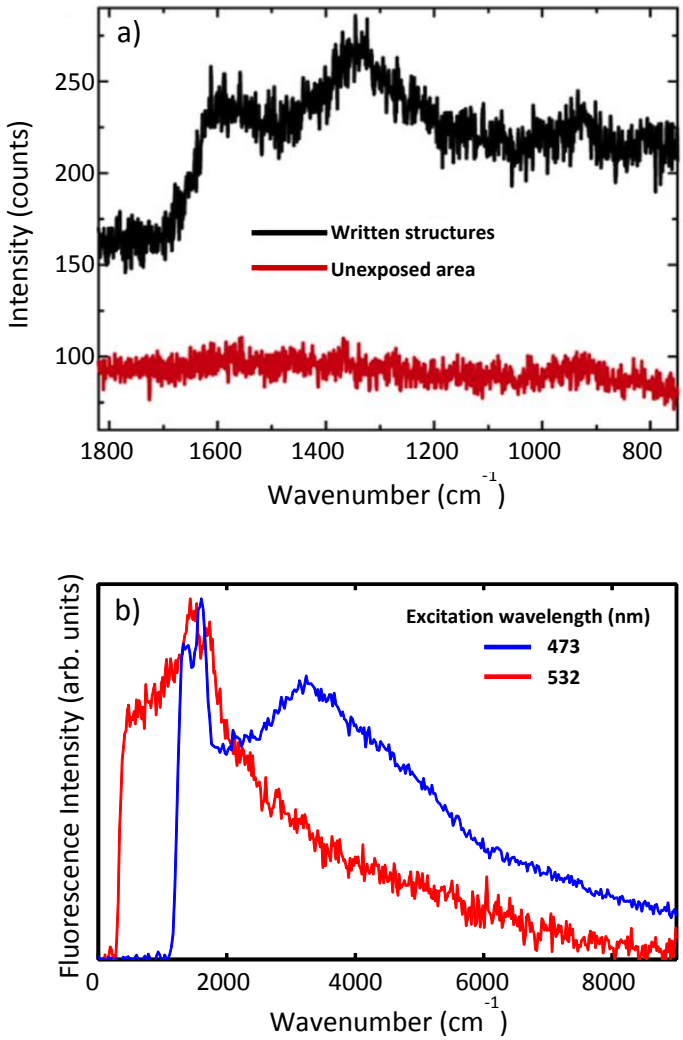

Figure 22: (a) Raman spectra detected from the written structures (black) in Ag@PMMA thin film, and unexposed areas (red) [5]. (b) Emission spectra detected from the written structures in Ag@PVA thin film excited with 473 nm (blue), and 532 nm (red) as a function of the Raman shift from the excitation light.

7.3 Bleaching parameters

In Chapter 6.5, the results of photobleaching experiments by recording the total emission intensity of the silver NCs after being excited with 473 nm and 532 nm excitation sources were reported. The photostability of the fabricated clusters can be studied by estimating the bleaching time constants of the structures excited with different laser wavelengths and intensities. As the fluorescence bleaching of the NCs was a two-fold exponential decay, the bleaching curves must be fitted by double exponential decay equation $y = a.\exp(-t/\tau_1) + b.exp(-t/\tau_2)$ with bleaching time constants τ_1 and τ_2, where a and b are amplitude parameters, and t is time. Figure 23 and Figure 24 indicate the exponential fits corresponding to the bleaching data of the written structures excited with different laser intensities of excitation wavelengths 473 nm and 532 nm, respectively. The bleaching time constants (τ_1 and τ_2) of the fluorescence signal were calculated from fitting parameters. Table 2 summarizes the acquired values for τ_1 and τ_2 when structures are excited with different wavelengths and intensities. Obtaining two different time constants for the bleaching process indicate that the fluorescence of NCs may decay by two different processes simultaneously. Both bleaching processes start at t = 0. However, the first process dyes out quite fast with time constant of τ_1. Then, the only process that governs the bleaching of the fluorescence is the slowly decaying process with time constant of τ_2. The origin of these two different processes cannot be determined with our current technique.

The values obtained for the second time constant (τ_2) confirm that fabricated luminescent NCs are remarkably photostable. Moreover, the photostability of them strongly depends on the excitation wavelength and intensity. For both excitation wavelengths, by increasing the irradiation intensity, the fluorescence signal decays considerably faster. Moreover, for a given excitation power, the fluorescence is more stable when the excitation wavelength is longer.

Table 2: Calculated bleaching time constants of written structures excited with 473 nm and 532 nm sources with three different intensities.

	λ_{exc} = 473 nm		λ_{exc} = 532 nm	
I_{exc} (MW/m^2)	τ_1 (s)	τ_2 (s)	τ_1 (s)	τ_2 (s)
0.6	102.6	990	22	1449
3	52	506.8	23	707.7
6	23	299.7	24.5	573.7

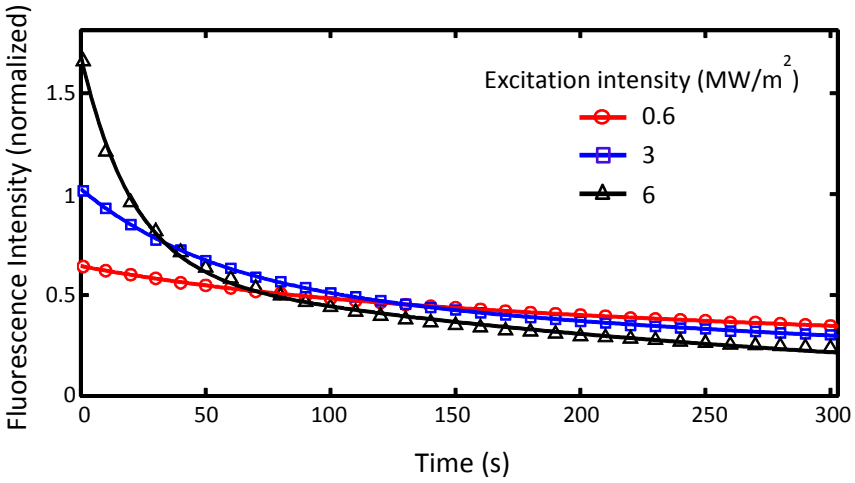

Figure 23: Fluorescence photobleaching curves corresponding to the structures excited with 473 nm excitation source, and I_{exc} of 0.6 MW/m^2(red), 3 MW/m^2(blue), and 6 MW/m^2(black). The solid lines represent double-exponential fits to the data points (open symbols).

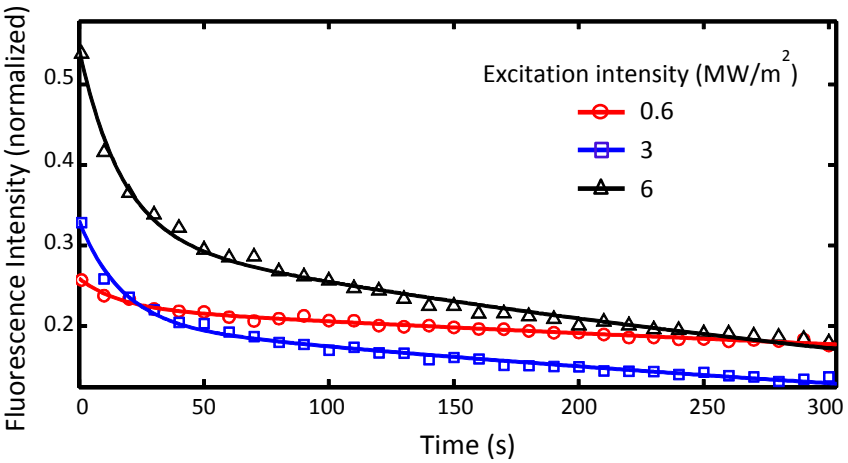

Figure 24: Fluorescence photobleaching curves corresponding to the structures excited with 532 nm excitation source, and I_{exc} of 0.6 MW/m^2(red), 3 MW/m^2(blue), and 6 MW/m^2(black). The solid lines represent double-exponential fits to the data points (open symbols).

Moreover, we observed when the samples were exposed to the 473 nm laser beam, the background region exhibits a considerable fluorescence signal which increases with time and incident beam intensity. Figure 25 shows the increase of the background fluorescence as a function of time for different excitation intensities. As the signal increases with laser intensity, it can be concluded that absorption of 473 nm light by silver-containing PVA induces the formation of silver NCs at the background region.

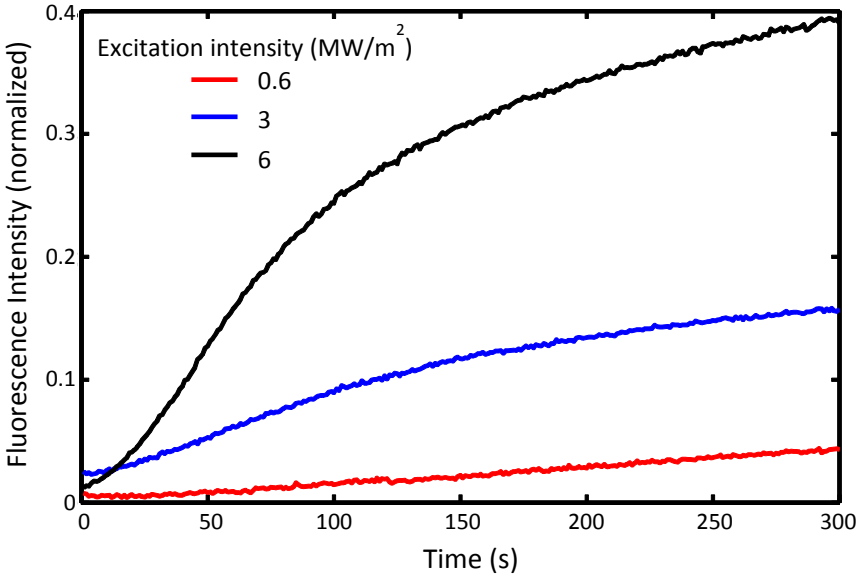

Figure 25: Total fluorescence intensity detected from the background area during 300 s time interval. The fluorescence signals were obtained by irradiating the sample with 473 nm excitation source and I_{exc} *of 0.6 MW/m*^{2}*(red), 3 MW/m*^{2}*(blue), and 6 MW/m*^{2}*(black).*

8. CONCLUSION

Nanoclusters as an intermediate state between atoms and nanoparticles exhibit significant optical, electronic, and chemical properties, which have made them attractive subjects of many studies during last decades. In this work, the major characteristics of metal nanoclusters with a focus on significant optical properties of noble metal NCs were studied. The physical principles of cluster growth and the need for stabilizing them in order to make benefit from their unique properties were described. Different modes of cluster stabilization by utilizing various stabilizing matrices were introduced and compared. Then, we focused on the features of polymers since they have been known as excellent stabilizers of colloids and clusters for a variety of applications. Notably, properties of PVA, the polymer matrix we utilized to grow and stabilize silver NCs, were explained. Physical process of polymerization and more specifically single and two-photon photo-induced polymerization techniques were introduced and compared.

Two-dimensional fluorescent microstructures with submicron line widths were fabricated by stabilizing silver NCs in silver containing PVA films utilizing single-photon DLW process using tightly focused beam of a 405 nm CW diode laser. Thin films of Ag@PVA with various concentrations of silver were prepared on glass substrates through spin-coating, and microstructures were written with different scanning speeds and laser writing intensities. Characterization of the samples was performed using AFM, bright-field microscopy, fluorescence microscopy, and fluorescence spectroscopy.

The thickness measurements of Ag@PVA films and fabricated structures indicated that DLW ablates a significant amount of material in the exposed areas. However, the obtained fluorescence profiles suggested that despite the material removal, silver NCs remain at the depth of the structures as the origin of the luminescence. Dependence of the fluorescence intensity emitted from the structures on the silver concentration was another evidence that the luminescence is due to the silver NCs stabilized by polymer molecules. Increasing the writing intensity showed the increment in line-width of the written microstructures, and consequently, enhancement of the total fluorescence intensity from the NCs. Along with the broadband fluorescence emission, a sharp peak was detected which is most likely attributed to an enhanced Raman scattering effect. Photostability of NCs was studied through several photobleaching tests, which were performed by irradiating the sample for 300 s and simultaneously recording the fluorescence intensity. Two different bleaching rates were observed indicated that the fluorescence decay is affected by two processes. The time constant corresponding to the

slow-decaying process reported on the substantial photostability of silver NCs. It was also observed that by varying the excitation wavelength and intensity, the photostability of the microstructures can be tuned. Larger excitation wavelengths and lower intensities lead to enhancing the photostability of NCs. Surprisingly, the regions without any written structures exhibited an increasing fluorescence signal under exposure to 473 nm excitation source suggesting the formation of NCs.

More investigations can be done to endorse some of the obtained results. Enhancement of the bright field microscopy might help visualizing the DLW on samples with very low and zero concentration of silver to further confirm that silver NCs are the only origin of the fluorescence. Moreover, the feasibility of working with lower silver concentrations might help to eliminate or decrease the probable clusters formation in the background region. Performing SEM-EDS analysis on written structures can ensure the presence of silver NCs in the exposed areas despite the material ablation. To further study the optical properties of NCs, the absorption and excitation spectra of the structures can be measured. Raman spectroscopy can be an effective investigation method in order to confirm that the narrow peak in the emission spectrum originates from enhanced Raman scattering. Furthermore, the behavior of the background region under excitation can be studied for longer time to investigate the mechanism of formation and photobleaching of NCs in background.

To sum up, our results showed that DLW can be a beneficial method to form and stabilize silver NCs in organic matrices. Strong photoluminescence and high photostability of the NCs fabricated by this method is comparable with those observed from NCs synthesized in solutions. A benefit of DLW is that it enables micropatterning of fluorescent structures in organic media using simple setups. Different kinds of polymer resins can be used as stabilizing scaffolds in this technique. Consistency of the luminescence and stability of fabricated NCs in PVA films with those of the femtosecond laser-written NC in PMMA films confirms that PVA is an appropriate matrix to form and stabilize silver NCs. Moreover, it shows that stable metal NCs can be fabricated by using cheap CW laser diodes. Therefore, this microfabrication process could be a promissing tool for applications such as bio-labeling, imaging, optical data storage, detection of metal ions, etc.

REFERENCES

[1] C. N. R. Rao, A. Müller and A. K. Cheetham, "Nanomaterials-an Introduction," in *The Chemistry of Nanomaterials*, John Wiley & Sons, 2006, pp. 1-11.

[2] H.-T. Sun and Y. Sakka, "Luminescent Metal Nanoclusters: Controlled Synthesis and Functional Applications," *Sci. Technol. Adv. Mater,* vol. 15, no. 1, 2014.

[3] P. Jena and A. W. Castleman Jr., "Introduction to Atomic Clusters," in *Nanoclusters*, Elsevier, 2010, pp. 1-28.

[4] C.-A. J. Lin, C.-H. Lee, J.-T. Hsieh, H.-H. Wang, J. K. Li, J.-L. Shen, W.-H. Chan, H.-I. Yeh and W. H. Chang, "Synthesis of Fluorescent Metallic Nanoclusters toward Biomedical Application: Recent Progress and Present Challenges," *Journal of Medical and Biological Engineering,* vol. 29, pp. 276-283, 2009.

[5] P. Kunwar, J. Hassinen, G. Bautista, R. H. A. Ras and J. Toivonen, "Direct Laser Writing of Photostable Fluorescent Silver Nanoclusters in Polymer Films," *ACS Nano,* vol. 8, p. 11165–11171, 2014.

[6] J. Zheng, J. T. Petty and R. M. Dickson, "High Quantum Yield Blue Emission from Water-Soluble Au8 Nanodots," *J. Am. Chem. Soc.*, vol. 125, no. 26, p. 7780–7781, 2003.

[7] E. G. Gwinn, P. O'Neill, A. J. Guerrero, D. Bouwmeester and D. K. Fygenson, "Sequence-Dependent Fluorescence of DNA-Hosted Silver," *Adv. Mater,* vol. 20, pp. 279-283, 2008.

[8] M. Bellec, A. Royon, K. Bourhis, J. Choi, B. Bousquet, M. Treguer, T. Cardinal, J.-J. Videau, M. Richardson and L. Canioni, "3D Patterning at the Nanoscale of Fluorescent Emitters in Glass," *J. Phys. Chem. C,* vol. 114, pp. 15584-15588, 2010.

[9] G. De Cremer, B. F. Sels, J.-i. Hotta, M. . B. J. Roeffaers, E. Bartholomeeusen, E. Coutiño-Gonzalez, V. Valtchev, D. E. De Vos, T. Vosch and J. Hofkens, "Optical Encoding of Silver Zeolite Microcarriers," *Advanced Materials,* vol. 22, no. 9, p. 957–960, 2010.

[10] T. Linnert, P. Mulvaney, A. Henglein and H. WeUer, "Long-Lived Nonmetallic Silver Clusters in Aqueous Solution: Preparation and Photolysis," *J. Am. Chem. Soc,* vol. 112, p. 46574664 , 1990.

[11] H. Xu and K. S. Suslick, "Water-Soluble Fluorescent Silver Nanoclusters," *Advanced Materials,* vol. 22, pp. 1078-1082, 2010.

[12] C. B. Arnold and A. Piqué, "Laser Direct-Write Processing," *MRS BULLETIN ,* vol. 32, pp. 9-15, 2007.

[13] I. Diez and R. H. A. Ras, "Fluorescent Silver Nanoclusters," *Nanoscale,* vol. 3, pp. 1963-1970, 2011.

[14] J. D. Aiken III and R. G. Finke, "A Review of Modern Transition-metal Nanoclusters: Their Synthesis, Characterization, and Applications in Catalysis," *Journal of Molecular Catalysis A: Chemical,* vol. 145, pp. 1-44, 1999.

[15] H. Bönnemann and K. S. Nagabhushana, "Metal Nanoclusters: Synthesis and

Strategies," in *Metal Nanoclusters in Catalysis and Materials Science*, Elsevier B.V., 2008, pp. 21-26.

[16] M. Faraday, "Experimental Relations of Gold (and other Metals) to Light," *The Royal Society,* vol. 147, pp. 145-181, 1857.

[17] L. Shang and S. Dong, "Facile Preparation of Water-soluble Fluorescent Silver Nanoclusters Using a Polyelectrolyte Template," *Chem. Commun,* no. 9, p. 1088–1090, 2008.

[18] M. S. El-Shall and A. S. Edelstein, "Formation of Clusters and Nanoparticles from a Supersaturated Vapor and Selected Properties," in *Nanomaterials: Synthesis, Properties and Applications*, Taylor & Francis Group, 1996, pp. 13-20.

[19] T. A. Ring, "Nano-sized Cluster Nucleation," *Advances in Colloid and Interface Science,* vol. 91, pp. 473-499, 2001.

[20] A. Fischer, R. Pagni, R. Compton and D. Kondepudi, "Laser Induced Crystallization," in *Nanoclusters,* Elsevier, 2010, pp. 343-356.

[21] H. M. Helmy, C. Ballhaus, R. O. Fonseca, R. Wirth, N. Thorsten and M. Tredoux, "Noble Metal Nanoclusters and Nanoparticles," *Nature Communications,* vol. 4, 2013.

[22] V. K. LaMer and R. H. Dinegar, "Theory, Production and Mechanism of Formation of Monodispersed Hydrosols," *J. Am. Chem. Soc.,* vol. 72, p. 4847–4854, 1950.

[23] J. Turkevich, P. C. Stevenson and J. Hillier, "A Study of the Nucleation and Growth Processes in the Synthesis of Colloidal Gold," *Discuss. Faraday Soc.,* vol. 11, pp. 55-75, 1951.

[24] A. E. Nielsen, Kinetics of Precipitation, Pergamon Press, 1964.

[25] E. E. Finney and R. G. Finke, "Nanocluster Nucleation and Growth Kinetic and Mechanistic Studies: A Review Emphasizing Transition-metal Nanoclusters," *Journal of Colloid and Interface Science,* vol. 317, p. 351–374, 2008.

[26] G. Schmid, in *Clusters and Colloids: From Theory to Applications,* John Wiley & Sons, 2008, pp. 1-6.

[27] G. Schmid, "General Features of Metal Nanoparticles Physics," in *Metal Nanoclusters in Catalysis and Materials Science*, Elsevier, 2008, pp. 3-19.

[28] L. J. De Jongh, "Metal-cluster Compounds: Model Systems for Nanosized Metal Particles," *Applied Organometallic Chemistry* , vol. 12, pp. 393-399, 1998.

[29] G. Schmid, "Quantum Dots," in *Nanoparticles*, Wiley-VCH, 2010, pp. 6-19.

[30] E. U. Rafailov, "Quantum Dot Technologies," in *The Physics and Engineering of Compact Quantum Dot-based Lasers for Biophotonics*, Wiley-VCH, 2014, p. 8.

[31] F. Janetzko, A. Goursot, T. Mineva, P. Calaminici, R. Flores-Moreno, A. M. Köster and D. R. Salahub, "Cluster Structures: Bridging Experiment and Theory," in *Nanoclusters*, Elsevier B.V., 2010, pp. 152-153.

[32] J. A. Alonso, "Electronic and Atomic Structure, and Magnetism of Transition-Metal Clusters," *Chemical Reviews,* vol. 100, pp. 637-677, 2000.

[33] O. Cheshnovsky, K. J. Taylor, J. Conceicao and R. E. Smalley, "Ultraviolet Photoelectron Spectra of Mass-selected Copper Clusters: Evolution of the 3d Band," *Phys. Rev. Lett.,* vol. 64, pp. 1785-1788, 1990.

[34] N. Fujima and T. Yamaguchi, "Shell Model and Magnetism of Transition-metal Microclusters," *Journal of Non-Crystalline Solids,* Vols. 117-118, pp. 285-288, 1990.

[35] C. Massobrio, A. Pasquarello and R. Car, "Structural and Electronic Properties Of Small Copper Clusters - A First Principles Study," *Chemical Physics Letters,* vol. 238, pp. 215-221, 1995.

[36] C. W. J. Bauschlicher, S. R. Langhoff and H. Partridge, "Theoretical Study of the Homonuclear Tetramers and Pentamers of the Group 1B Metals (Cu, Ag, and Au)," *J. Chem. Phys.,* vol. 93, pp. 8133-8137, 1990.

[37] K. Michaelian, N. Rendón and I. L. Garzón, "Structure and Energetics of Ni, Ag, and Au Nanoclusters," *Phys. Rev. B,* vol. 60, pp. 2000-2010, 1999.

[38] D. L. Fedlheim and C. A. Foss, in *Metal Nanoparticles: Synthesis, Characterization, and Applications*, CRC Press, 2001, pp. 1-22.

[39] R. H. Magruder III, L. Yang, R. F. Haglund Jr., C. W. White, L. Yang, R. Dorsinville and R. R. Alfano, "Optical Properties of Gold Nanocluster Composites Formed by Deep Ion Implantation in Silica," *Applied Physics Letters,* vol. 62, pp. 1730-1732, 1993.

[40] J. Zheng, C. Zhang and R. M. Dickson, "Highly Fluorescent,Water-Soluble, Size-Tunable Gold Quantum Dots," *Physical Review Letters,* vol. 93, 2004.

[41] Y. Lu and W. Chen, "Size Effect of Silver Nanoclusters on Their Catalytic Activity for Oxygen Electro-reduction," *Journal of Power Sources,* vol. 197, pp. 107-110, 2012.

[42] X. Le Guével, B. Hötzer, G. Jung, K. Hollemeyer, V. Trouillet and M. Schneider, "Formation of Fluorescent Metal (Au, Ag) Nanoclusters Capped in Bovine Serum Albumin Followed by Fluorescence and Spectroscopy," *Phys. Chem. C,* vol. 115, p. 10955–10963, 2011.

[43] J. Zheng, Y. Ding, B. Tian, Z. L. Wang and X. Zhuang, "Luminescent and Raman Active Silver Nanoparticles with Polycrystalline," *J. AM. CHEM. SOC.,* vol. 130, p. 10472–10473, 2008.

[44] K. Kneipp, "Surface-enhanced Raman Scattering," *Physics Today,* vol. 31, pp. 40-46, 2007.

[45] F. Klasovsky and P. Claus, "Metal Nanoclusters in Catalysis: Effects of Nanoparticle Size, Shape, and Structure," in *Metal Nanoclusters in Catalysis and Materials Science*, Elsevier B.V. , 2007, pp. 167-177.

[46] P. B. Armentrout, "Reactivity and Thermochemistry of Transition Metal Cluster Cations," in *Nanoclusters*, Elsevier B.V., 2010, pp. 269-270.

[47] J. Li, J.-J. Zhu and K. Xu, "Fluorescent Metal Nanoclusters: From Synthesis to Applications," *Trends in Analytical Chemistry,* vol. 58, pp. 90-98, 2014.

[48] G. Schmid and L. F. Chi, "Metal Clusters and Colloids," *Advanced Materials,* vol. 10, pp. 515-526, 1998.

[49] J. T. Petty, J. Zheng, N. V. Hud and R. M. Dickson, "DNA-Templated Ag Nanocluster Formation," *J. AM. CHEM. SOC. 2,* vol. 126, pp. 5207-5212, 2004.

[50] T. Vosch, Y. Antoku, J.-C. Hsiang, C. I. Richards, J. I. Gonzalez and R. M. Dickson, "Strongly Emissive Individual DNA-encapsulated Ag Nanoclusters as Single-molecule Fluorophores," *Proceedings of the National Academy of Sciences of the United States of America,* vol. 104, pp. 12616-12621, 2007.

[51] Y. Bao, C. Zhong, D. M. Vu, J. P. Temirov, R. B. Dyer and J. S. Martinez, "Nanoparticle-Free Synthesis of Fluorescent Gold Nanoclusters at Physiological Temperature," *J. Phys. Chem. C,* vol. 111, pp. 12194-12198, 2007.

[52] C. I. Richards, S. Choi, J.-C. Hsiang, Y. Antoku, T. Vosch, A. Bongiorno, Y.-L. Tzeng and R. M. Dickson, "Oligonucleotide-Stabilized Ag Nanocluster Fluorophores," *J. AM. CHEM. SOC.*, vol. 130, p. 5038–5039, 2008.

[53] J. Zhang, S. Xu and E. Kumacheva, "Photogeneration of Fluorescent Silver Nanoclusters in Polymer Microgels," *Advanced Materials,* vol. 17, pp. 2336-2340, 2005.

[54] C. E. Carraher, "Introduction to Polymer Science and Technology," in *Applied Polymer Science: 21st Century*, Elsevier, 2000, pp. 21-26.

[55] T. Fuller, "Introductory Consepts and Definitions," in *The Elements of Polymer Science & Engineering*, Academic Press, 2012, pp. 1-22.

[56] D. W. Van Krevelen and K. T. Nijenhuis, "Typology of Polymers," in *Properties of Polymers*, Elsevier, 2009, pp. 7-8.

[57] M. Rubinstein and R. H. Colby, in *Polymer Physics*, Oxford University Press, 2003, pp. 9-15.

[58] A. Rudin and P. Choi, "Step-Growth Polymerizations," in *The Elements of Polymer Science & Engineering*, Academic Press, 2012, pp. 305-310.

[59] D. H. Napper, "Polymeric Stabilization of Colloidal Dispersions," *British Polymer Journal,* vol. 18, p. 278, 1986.

[60] J. Wang and L. Ye, "Structure and Properties of Polyvinyl alcohol/Polyurethane Blends," *Composites Part B: Engineering,* vol. 69, pp. 389-396, 2014.

[61] J. Pajak, Z. Michal and N. Bozena, "Poly(vinyl alcohol) – Biodegradable Vinyl Material," *Chemik,* vol. 64, pp. 523-530, 2010.

[62] C. M. Hassan and N. A. Peppas, "Structure and Applications of Poly (vinyl alcohol) Hydrogels Produced by Conventional Crosslinking or by Freezing/Thawing Methods," *Advances in Polymer Science,* vol. 153, pp. 37-65, 2000.

[63] M. I. Baker, S. P. Walsh, Z. Schwartz and B. D. Boyan, "A Review of Polyvinyl alcohol and its Uses in Cartilage and Orthopedic Applications," *J Biomed Mater Res Part B,* vol. 100, pp. 1451-1457, 2012.

[64] R. Chandra and R. Rustigi, "Biodegradable Polymers," *Prog. Polym. Sci,* vol. 23, p. 1273–1335, 1998.

[65] B. J. Hollan and J. N. Hay, "The Thermal Degradation of Poly(vinyl alcohol)," *Polymer,* vol. 42, pp. 6775-6783, 2001.

[66] R. Olayo, E. Garcia, B. Garcia-Corichi, L. Sanchez-Vazquez and J. Alvarez, "Poly (vinyl alcohol) as a Stabilizer in the Suspension Polymerization of Styrene: The Effect of the Molecular Weight," *Journal of Applied Polymer Science*, vol. 67, p. 71–77, 1998.

[67] S. Ghoshal, P. Denner, S. Stapf and C. Mattea, "Study of the Formation of Poly(vinyl alcohol) Films," *Macromolecules,* vol. 45, pp. 1913-1923, 2012.

[68] M. Xanthos, "Polymer Processing," in *Applied Polymer Science: 21st Century*, Elsevier, 2000, pp. 355-371.

[69] B. D. Hall, P. Underhill and J. M. Torkelson, "Spin Coating of Thin and Ultrathin Polymer Films," *Polymer Engineering and Science,* vol. 38, pp. 2039-2045, 1998.

[70] N. Sahu, B. Parija and S. Panigrahi, "Fundamental Understanding and Modeling of Spin Coating Process : A Review," *Indian J. Phys.,* vol. 83, no. 4, pp. 493-502, 2009.

[71] W. W. Flack, D. S. Soong, A. T. Bell and D. W. Hess, "A Mathematical Model for Spin Coating of Polymer Resists," *J. AppJ. Phys.*, vol. 56, pp. 1199-1206, 1984.

[72] H. B. Sun and S. Kawata, "Two-Photon Photopolymerization and 3D Lithographic Microfabrication," in *NMR, 3D Analysis, Photopolymerization*, vol. 170, Springer-Verlag: APS, 2004, pp. 170-239.

[73] A. Ostendorf and B. N. Chichkov, "Two-Photon Polymerization: A New Approach to Micromachining," *Photonics Spectra,* pp. 72-80, 2006.

[74] D. W. Van Krevelen and K. T. Nijenhuis, "Thermal Decomposition, Chemical Degradation," in *Properties of Polymers*, Elsevier, 2009, pp. 763-786.

[75] R. Premraj and M. Doble, "Biodegradation of Polymers," *Indian Journal of Biotechnology,* vol. 4, pp. 186-193, 2005.

[76] Z. Peng and L. X. Kong, "A Thermal Degradation Mechanism of Polyvinyl alcohol/Silica," *Polymer Degradation and Stability,* vol. 92, pp. 1061-1071, 2007.

[77] D. M. Larking, R. J. Crawford, G. B. Y. Christie and G. T. Lonergan, "Enhanced Degradation of Polyvinyl Alcohol by Pycnoporus cinnabarinus after Pretreatment with Fenton's Reagent," *Applied and Environmental Microbiology,* p. 1798–1800, 1999.

[78] M. A. Tehfe, F. Louradour, J. Lalevée and J.-P. Fouassier, "Photopolymerization Reactions: On the Way to a Green and Sustainable Chemistry," *Appl. Sci.,* vol. 3, pp. 490-514, 2013.

[79] J. P. Fouassier, X. Allonas and D. Burget, "Photopolymerization Reactions Under Visible Lights: Principle, Mechanisms and Examples of Applications," *Progress in Organic Coatings,* vol. 47, pp. 16-36, 2003.

[80] A. Ovsianikov, A. Ostendorf and B. N. Chichkov, "Three-dimensional Photofabrication with Femtosecond Lasers for Applications in Photonics and Biomedicine," *Applied Surface Science,* vol. 253, p. 6599–6602, 2007.

[81] Y. Yagci, S. Jockusch and N. J. Turro, "Photoinitiated Polymerization: Advances, Challenges, and Opportunities," *Macromolecules,* vol. 43, p. 6245–6260, 2010.

[82] T. E. Long and S. R. Turner, "Step-growth Polymerization," in *Applied Polymer Science: 21st Century*, Elsevier, 2000, pp. 979-981.

[83] F. J. Davis, in *Polyemer Chemistry*, Oxford University Press, 2004, pp. 41-127.

[84] K. Matyjaszewski and S. G. Gaynor, "Free Radical Polymerization," in *Applied Polymer Science: 21st Century*, Elsevier, 2000, p. 929–977.

[85] J. J. Serbin, in *Fabrication of Photonic Structures by Two-Photon Polymerization*, Cuvillier Verlag, 2004, pp. 5-7.

[86] S. Chatani, C. J. Kloxin and C. N. Bowman, "The Power of Light in Polymer Science: Photochemical Processes to Manipulate Polymer Formation, Structure, and Properties," *Polym. Chem,* vol. 5, pp. 2187-2201, 2014.

[87] M. T. Do, Q. Li, T. T. N. Nguyen, H. Benisty, I. Ledoux-Rak and D. N. Lai, "High Aspect Ratio Submicrometer Two-dimensional Structures Fabricated by One-photon Absorption Direct Laser Writing," *Microsystem Technologies,* vol. 20, no. 143, p. 2097–2102, 2014.

[88] S. Maruo and K. Ikuta, "Three-dimensional Microfabrication by Use of Single-Photon-Absorbed Polymerization," *Appl. Phys. Lett.,* vol. 76, no. 19, pp. 2656-2658, 2000.

[89] S. Maruo and K. Ikuta, "Submicron Stereolithography for the Production of Freely

Movable Mechanisms by Using Single-Photon Polymerization," *Sensors and Actuators A,* vol. 100, pp. 70-76, 2002.

[90] A. S. Kewitsch and A. Yariv, "Self-focusing and Self-trapping of Optical Beams upon Photopolymerization," *OPTICS LETTERS,* vol. 21, no. 1, pp. 24-26, 1996.

[91] S. Kawata and H.-B. Sun, "Two-Photon Photopolymerization as a Tool for Making Micro-Devices," *Applied Surface Science,* Vols. 153-158, pp. 208-209, 2003.

[92] W. Kaiser and C. G. B. Garrett, "Two-Photon Excitation in CaF2: Eu2+," *Phys. Rev. Lett.,* vol. 7, no. 229, pp. 229-231, 1961.

[93] Y. H. Pao and P. M. Rentzepis, "Laser-Induced Production of Free Radicals in Organic Compounds," *Appl Phys Lett,* vol. 6, no. 93, pp. 93-95, 1965.

[94] S. Maruo, O. Nakamura and S. Kawata, "Three-dimensional Microfabrication with Two-Photon-Absorbed Photopolymerization," *Optics Letters,* vol. 22, no. 2, pp. 2656-2658, 1997.

[95] N. C. Strandwitz, A. Khan, S. W. Boettcher, A. A. Mikhailovsky, C. J. Hawker, T.-Q. Nguyen and G. D. Stucky, "One- and Two-Photon Induced Polymerization of Methylmethacrylate Using Colloidal CdS Semiconductor Quantum Dots," *J. AM. CHEM. SOC.,* vol. 130, p. 8280–8288, 2008.

[96] J. Zheng, Y. ding, B. Tian, Z. L. Wang and X. Zhuang, "Luminescent and Raman Active Silver Nanoparticles with Polycrystalline Structure," *J. AM. CHEM. SOC.,* vol. 130, p. 10472–10473, 2008.

[97] L. Peyser-Capadona, J. Zheng, J. I. Gonzalez, L. Tae-Hee, S. A. Patel and R. M. Dickson, "Nanoparticle-Free Single Molecule Anti-Stokes Raman Spectroscopy," *Phys. Rev. Lett.,* vol. 94, no. 5, 2005.